



ITN-5VC

Integrated Telematics for Next Generation 5G Vehicular Communications

ITN-5VC D1.4

Optimized on-road performance of phased arrays for sensors – A Numerical Simulation Analysis

Version v3.0

Date: 2025/01/29

Document properties:

Grant Number:	955629
Document Number:	D1.4
Document Title:	Optimized on-road performance of phased arrays for sensors – A Numerical Simulation Analysis
Partners involved:	TUIL, UT
Authors:	Aamir Ullah Khan, Alejandro Antón Ruiz, and Andrés Alayón Glazunov (Editor)
Contractual Date of Delivery:	2025/01/31
Dissemination level:	PU ¹
Version:	3.0
File Name:	ITN-5VC D1.4_v3.0

¹ CO = Confidential, only members of the consortium (including the Commission Services)

PU = Public

Table of Contents

Executive summary	5
List of figures	6
List of tables	7
List of acronyms and abbreviations	8
1 Introduction	9
1.1 Integrated Sensing and Communication	9
1.2 Vehicle-to-Vehicle Communications	10
2 Propagation Model.....	10
2.1 Characteristics of an ISAC Propagation Model.....	10
2.2 Proposed ISAC Propagation Model	11
2.2.1 Direct Link (DL)	11
2.2.2 Indirect Link via Dynamic Targets (IDL-DTs).....	12
2.2.3 Indirect Link via Diffuse Scatterers (IDL-DI)	12
2.2.4 Overall Channel Response.....	12
3 Simulation Setup	13
3.1.1 Road Layout and Diffuse (DI) Scatterers Distribution	13
3.1.2 Vehicle Positioning and Trajectory.....	13
3.1.3 Simulation Tools.....	13
4 Multiple Antennas for ISAC enabled V2V setup.....	13
4.1 Antenna Placement Schemes.....	14
4.1.1 Front Bumper (FB) Setup	14
4.1.2 Back Bumper (BB) Setup	14
4.1.3 Combined Gain Pattern (CGP) setup.....	14
4.2 Radiation Patterns	15
4.2.1 Horn Antenna.....	16
4.2.2 Patch Antenna.....	16
4.2.3 Phased Array Antenna Element	16
4.2.4 Phased Array Configurations.....	17
5 Simulation Parameters and Results Discussion	18
5.1 Figures of Merit (FoMs)	19
5.2 Horn Antenna	19
5.2.1 Channel Magnitude of DL, Joint DTs, and DI Scatterers	19
5.2.2 Overall Channel Magnitude	21
5.2.3 Target Detection	22
5.3 Patch Antenna	23

5.3.1	Channel Magnitude of DL, Joint DTs, and DI Scatterers	23
5.3.2	Overall Channel Magnitude	24
5.3.3	Target Detection	26
5.4	Phased Array Antenna Element	27
5.4.1	Channel Magnitude of DL, Joint DTs, and DI Scatterers	27
5.4.2	Overall Channel Magnitude	28
5.4.3	Target Detection	29
5.5	Statistical Characteristics of Different Placement Schemes.....	31
5.6	Phased Arrays	33
5.6.1	Channel Magnitude of DL, Joint DTs, and DI Scatterers	33
5.6.2	Overall Channel Magnitude	34
5.6.3	Target Detection	35
5.6.4	Statistical Characteristics of Different Phased Arrays.....	38
6	Conclusion	40
	References.....	42

Executive summary

The deliverable outlines a comprehensive investigation into the performance optimization of phased array antennas for Integrated Sensing and Communication (ISAC)-enabled Vehicle-to-Vehicle (V2V) communication systems, focusing on a highway environment. The study integrates a novel propagation model tailored for ISAC, which accommodates both radar sensing and wireless communication functionalities. Simulations were conducted using a variety of antenna types (horn, patch, phased arrays) and configurations, considering factors such as antenna placement and radiation patterns. Key metrics such as channel magnitude and target detection accuracy were evaluated under different scenarios, including single antenna and phased array setups.

Phased arrays emerged as a critical innovation due to their ability to provide enhanced directional gain, flexibility in beam steering, and improved target detection accuracy. In this regard, D1.1 and D1.3 have explored the design and manufacture of phased arrays for automotive applications, with the main focus on sensing, while D1.2 has focused on the characterization of phased arrays for automotive applications. This deliverable aims at complementing WP1 work by providing insights on the simulation of ISAC-enabled V2V scenarios to quantify the impact on performance of different antenna solutions, including phased arrays.

In particular, results show that the Combined Gain Pattern (CGP) configuration demonstrated superior performance compared to front and rear bumper setups. Moreover, larger phased arrays with finer beam steering resolution (5°) consistently outperformed smaller arrays and setups with coarser resolutions (10°), resulting in higher channel magnitudes and more reliable target detection.

The study underscores the importance of incorporating diffuse scatterers in the propagation model to accurately simulate real-world environments. It also highlights phased arrays as a cornerstone for future ISAC-enabled V2V systems to achieve reliable communication and sensing. Part of the results presented in this report have been summarized in papers [15], [16], which have been presented at WCNC 2024 and VNC 2024, respectively.

List of figures

Figure 1. ISAC use cases. From https://newshub.sustech.edu.cn/en/html/202301/38318.html	9
Figure 2. Geometry of the road and distribution of DI scatterers	11
Figure 3. Omnidirectional Tx and front bumper setup	14
Figure 4. Omnidirectional Tx and back bumper setup	14
Figure 5. Omnidirectional Tx and CGP setup	15
Figure 6. Car model with specified antenna locations	15
Figure 7. Antenna gain of horn antenna in different setups.....	16
Figure 8. Antenna gain of patch antenna in different setups.	16
Figure 9. Antenna gain of phased array AE in different setups	17
Figure 10. Antenna gain of phased arrays of 4, 8, and 16 AEs, with 5° and 10° beam steering resolution angles	18
Figure 11. Horn antenna: Channel magnitude of DL, joint DTs, and DI scatterers	20
Figure 12. Horn antenna: Overall channel magnitude	21
Figure 13. Horn antenna: Target detection snapshot at 12s	23
Figure 14. Horn antenna: Target detection snapshot at 14s	23
Figure 15. Patch antenna: Channel magnitude of DI, joint DTs, and DI scatterers.....	24
Figure 16. Patch antenna: Overall channel magnitude.....	25
Figure 17. Patch antenna: Target detection snapshot at 12s	27
Figure 18. Patch antenna: Target detection snapshot at 14s	27
Figure 19. Phased array AE: Channel magnitude of DL, joint DTs, and DI scatterers	28
Figure 20. Phased array AE: Overall channel magnitude	29
Figure 21. Phased array AE: Target detection snapshot at 12s	30
Figure 22. Phased array AE: Target detection snapshot at 14s	31
Figure 23. Phased arrays: Channel magnitude of DL, joint DTs, and DI scatterers.....	34
Figure 24. Phased arrays: Channel magnitude of DL, joint DTs, and DI scatterers.....	34
Figure 25. Phased arrays: Overall channel magnitude.....	35
Figure 26. Phased arrays: Target detection snapshot at 11.46s	37
Figure 27. Phased arrays: Target detection snapshot at 13.56s	38

List of tables

Table 1. Simulation Parameters	18
Table 2. DT detection rate for horn antenna setup	22
Table 3. DT detection rate for patch antenna setup.....	26
Table 4. DT detection for phased array AE.....	30
Table 5. Statistical properties of different placement schemes	32
Table 6. DT detection rate for different phased arrays	36
Table 7. Statistical properties of different phased arrays.....	40

List of acronyms and abbreviations

ADAS	Advanced Driver Assistance Systems
AE	Antenna Element
CDF	Cumulative Distribution Function
CGP	Combined Gain Pattern
DI	Diffuse
DL	Direct Link
DR	Detection Rate
DT	Dynamic Target
FoM	Figure of Merit
GBSCM	Geometry-based Stochastic Channel Model
IDL	Indirect Link
IDL-DI	Indirect Link via Diffuse Scatterers
IDL-DT	Indirect Link via Dynamic Targets
IES	Inter-Element Spacing
ITS	Intelligent Transportation Systems
ISAC	Integrated Sensing and Communication
KPI	Key Performance Indicator
LOS	Line-Of-Sight
MIMO	Multiple-Input Multiple-Output
RCS	Radar Cross Section
RSU	Roadside Unit
Rx	Receiver
SC	Selection Combining
SCM	Spatial Channel Model
SINR	Signal to Interference plus Noise Ratio
SNR	Signal to Noise Ratio
SUMO	Simulation of Urban MObility
Tx	Transmitter
ULA	Uniform Linear Array
V2V	Vehicle to Vehicle
WP1	Work Package 1

1 Introduction

Work Package 1 (WP1) aims at providing antenna design and characterization for both radar and communications in the automotive context, with phased array antennas being of special interest. This is reflected in D1.1 and D1.3 being focused on the design and manufacturing of phased arrays, while D1.2 is focused on their characterization in testing environments. However, this characterization includes not only the testing methodologies of the antennas and systems, but also the development of channel models that can be used for system performance simulations. Here, the focus is on the Integrated Sensing and Communication (ISAC) framework within the ITN-5VC project context.

This deliverable presents a channel model for ISAC, which is used to evaluate the impact on system performance using several antennas designs and configurations in an automotive environment. Performance gains achievable by resorting to the use of phased arrays are highlighted.

1.1 Integrated Sensing and Communication

Next generation wireless networks (beyond 5G, e.g., 6G) are anticipated to play a pivotal role in enabling a wide range of emerging applications. Such emerging applications not only require high data rates and reliability but also need robust sensing capability. It is estimated that radar sensing will play an even more crucial role in these emerging technologies than it did in the past [1]. Over the years, wireless communications and radar sensing have advanced in their respective domains with little to no overlap. However, both technologies share many underlying similarities such as signal processing algorithms, propagation medium and mechanisms, devices, and to a certain extent hardware architecture [2].

Integrated Sensing and Communication (ISAC) is an intriguing emerging research area that combines radar sensing and communication functionalities in a unified platform, capitalizing on shared aspects of signal processing, spectrum utilization, and system design. The goal of ISAC is to unify radar sensing and wireless communication operations under a single platform. The aim of ISAC systems is to explore direct trade-offs and optimize the mutual performance gains of radar sensing and wireless communication. Envisioned use cases are illustrated in Fig.1, where automotive applications are highlighted as vehicle to everything applications [3],[4].

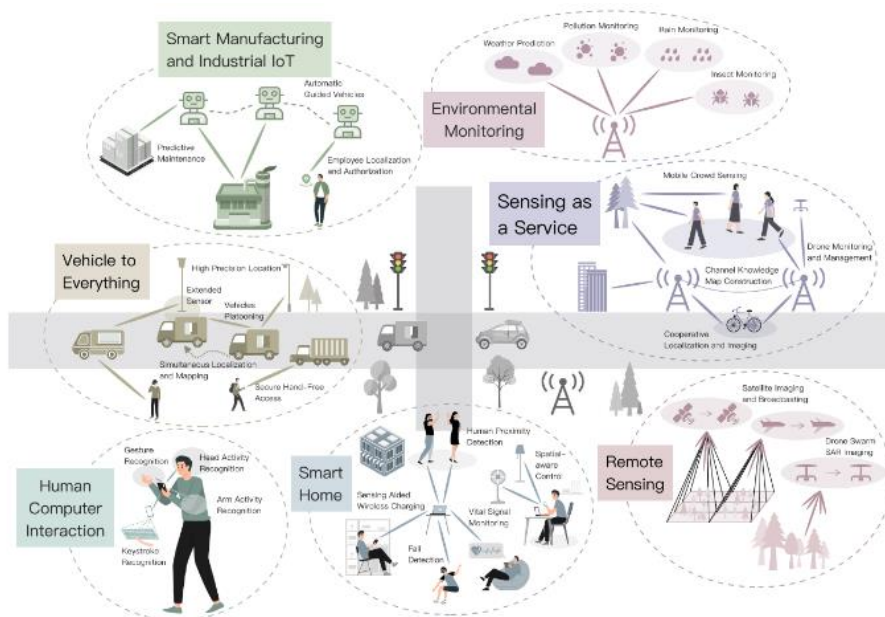


Figure 1. ISAC use cases. From <https://newshub.sustech.edu.cn/en/html/202301/38318.html>

ISAC can significantly improve spectrum utilization and mitigate the spectrum conflict between radar and wireless communication systems. By integrating the radar sensing and communication functionalities within a single device or network infrastructure, ISAC helps reduce hardware size, lower signal processing costs, and improve energy consumption [3], [4].

1.2 Vehicle-to-Vehicle Communications

One of the most vital applications of ISAC lies within the vehicular environment. The ISAC-enabled Vehicle to Vehicle (V2V) setups are essential for the future Intelligent Transportation Systems (ITS); however, they represent a challenging application scenario that requires a rigorous approach. For example, it is possible to utilize the currently deployed Roadside Units (RSUs) for radar sensing with only minor modifications to the hardware and communication strategies. This adaptation enables ISAC to facilitate connectivity between vehicles, as well as with infrastructure and networks. ISAC-enabled V2V setups can lead to more reliable position information and better communication quality, which results in improved traffic scenarios (fewer traffic jams, decreased rates of accidents [5], [6].

However, ISAC-enabled V2V systems are still in their infancy. Designing effective, performance- and cost-efficient and ISAC-enabled V2V systems requires a thorough understanding of the propagating characteristics of the radio channel. Devising realistic and representative ISAC-enabled V2V propagation channel models is critical for effective design, performance assessment, and standardization [7].

2 Propagation Model

In the past two decades, various channel models for traditional V2V communications have been proposed. These include standardized models such as COST action projects, 3GPP Spatial Channel Model (SCM) [8], WINNER channel model [9], IEEE 802.11p, and IEEE 802.11bd [10]. Moreover, extensive measurements have been conducted for channel modeling in various experimental setups including highway, urban, rural, crossroad, and street intersections [11], [12]. These channel models focus on different aspects of the vehicular environment, including antenna placement, radiation patterns, and the polarization of both transmitting and receiving antennas. However, traditional V2V channel models fail to meet the stringent reliability and accuracy requirements of ISAC-enabled V2V systems. In ISAC, radar sensing and communication takes place simultaneously. Therefore, dedicated propagation models are necessary to be developed for ISAC-enabled V2V systems.

2.1 Characteristics of an ISAC Propagation Model

As radar sensing and wireless communication are integrated into a unified platform, the characteristics of the propagation channel for ISAC-enabled V2V systems differ significantly from those of traditional V2V channels. It involves the signal transmission from the communication Transmitter (Tx) to the communication Receiver (Rx), along with the echo propagation from the sensing Tx to the scatterers, which are then received by the sensing Rx. This makes ISAC-enabled V2V channels more susceptible to the surrounding environment, including moving vehicles, pedestrians, and scatterers [13], [14]. The abundance of scatterers in the surrounding environment leads to significant multipath effects and clutter, characterized by a rapid birth and death process. Due to the high-speed mobility of vehicles and scatterers distributions in the environment, time-varying channel behavior must be modelled in ISAC-enabled V2V channels for both communication and sensing components. These factors make channel modeling of ISAC-enabled V2V systems a highly challenging task.

2.2 Proposed ISAC Propagation Model

As the characteristics, properties, and requirements of the ISAC propagation model are inherently different from the traditional V2V propagation models, they cannot be used in their current formulations for ISAC-enabled V2V systems. For a proper ISAC-enabled V2V system, new propagation models or modifications to the existing V2V propagation models are necessary to meet the new stringent requirements.

Based on the above analysis, an ISAC-extended propagation model for the highway scenario is presented in [15]. For the proposed model, an existing V2V propagation model [12] is modified to incorporate radar sensing by integrating vehicles' Radar Cross Section (RCS). Our extended channel model suits ISAC systems performing communication and radar sensing simultaneously, thus realizing an ICAS channel model. The model only considered omnidirectional radiation patterns for the transmitting and receiving antennas. This served as a limitation of the model for applications where directivity plays a significant role, as it does not fully account for the directional characteristics of the antennas or the impact of beam alignment on performance. The proposed model is further extended in [16] by incorporating a directive Rx with various antenna radiation patterns and placements, enabling an investigation into the effects of antenna placement on channel performance and target detection capability. The channel impulse response (CIR) is given as [16]:

$$h(t) = \sum_s g_{Tx}(\theta = 0, \phi_s) g_{Rx}(\theta = 0, \phi_s) \gamma_s e^{j2\pi\alpha_s t} \delta(t - \tau_s), \quad (1)$$

where τ_s and α_s represent the excess delay and Doppler shift of the respective path s . On the other hand, g_{Tx} is the Tx amplitude gain, for which a constant value of 1.5 dB is considered, which is equivalent to a power gain of 3 dB. The Rx has an amplitude gain g_{Rx} , which is dependent on ϕ_s , varying differently depending on the considered radiation pattern (see Section 4.2). Please note that, whenever a gain is presented with G , it is a power gain, while if it is presented with a g , then it is an amplitude gain. The relationship, in linear scale, is $g = \sqrt{G}$. The amplitude of path s is represented by γ_s . We have considered three major contributors to the overall channel response in our simulations: the direct link (DL), the indirect link via dynamic targets (IDL-DT), and the indirect link via diffuse scatterers (IDL-DI), which are indicated in Fig. 2 by the red line, the blue line, and the green line, respectively.

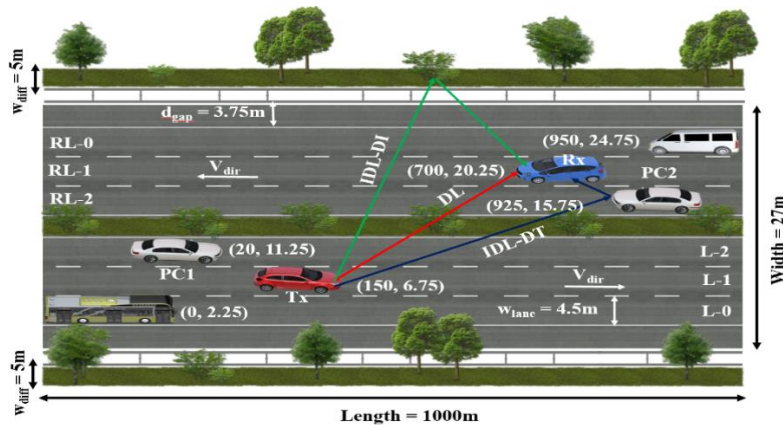


Figure 2. Geometry of the road and distribution of DI scatterers

The mathematical models and the components of each of the signal contributions are explained next.

2.2.1 Direct Link (DL)

The DL component defines the link between Tx and Rx when no vehicles or obstacles are blocking the path. The DL channel response is given by:

$$h_{DL}(t) = g_{Tx} g_{Rx} \gamma_{DL} e^{j2\pi\alpha_{DL}t} \delta(t - \tau_{DL}), \quad (2)$$

where α_{DL} and τ_{DL} represent the Doppler shift and delay for the DL component. The amplitude γ_{DL} is given by:

$$\gamma_{DL} = P_{ref,DL}^{1/2} \left(\frac{d_{ref}}{d_{Tx \rightarrow Rx}} \right)^{n_{DL}/2}, \quad (3)$$

where $P_{ref,DL}$ and n_{DL} represent the reference power and path-loss exponent for the DL. The DL distance between Tx and Rx is represented by $d_{Tx \rightarrow Rx}$. The delay and Doppler shift mathematical expressions for the DL component are given in (4) and (5) of [15].

2.2.2 Indirect Link via Dynamic Targets (IDL-DTs)

IDL-DTs components refer to the Indirect Link (IDL), which results from other moving vehicles on the road, i.e., Tx \rightarrow k \rightarrow Rx (where k denotes the kth DT). The IDL-DTs channel response can be mathematically expressed as [16]:

$$h_{DT}(t) = \sum_{k=1}^K g_{(Tx,k)} g_{(Rx,k)} \gamma_k e^{j2\pi\alpha_k t} \delta(t - \tau_k), \quad (4)$$

where α_k and τ_k represent the Doppler shift and delay for the kth DT. K is the total number of DT components in our scenario. The amplitude γ_k is given by:

$$\gamma_k = P_{ref,k}^{1/2} \left(\frac{d_{ref}}{d_{Tx \rightarrow k}} \right)^{n_k/2} \sqrt{\frac{\sigma_{RCS,k}}{4\pi(d_{k \rightarrow Rx})^{n_k}}}, \quad (5)$$

where $P_{ref,k}$ is the reference power for the kth DT and n_k is the path-loss exponent. $d_{Tx \rightarrow k}$ and $d_{k \rightarrow Rx}$ represent the distance from Tx to kth DT and kth DT to Rx, respectively. The overall link distance is called bistatic distance indicated by d_{bi} . Radar Cross Section (RCS) of the kth DT is denoted by $\sigma_{RCS,k}$. The delay and Doppler shift mathematical expressions for the IDL-DTs are given in (8) and (9) of [15].

2.2.3 Indirect Link via Diffuse Scatterers (IDL-DI)

The DI scatterers represent the point scatterers or vegetation on both sides of the road. The link from these point scatterers (Tx \rightarrow q \rightarrow Rx) depicts IDL-DI scatterers. Here q denotes the qth diffuse scatterer. The DI channel response can be mathematically expressed as:

$$h_{DI}(t) = \sum_{q=1}^Q g_{(Tx,q)} g_{(Rx,q)} \gamma_q e^{j2\pi\alpha_q t} \delta(t - \tau_q), \quad (6)$$

where α_q and τ_q represent the Doppler shift and delay for the qth DI scatterer. Q is the total number of DI scattering components in our scenario. The amplitude γ_q of the amplitude of DI scatterer is modeled according to the classical Geometry-based Stochastic Channel Model (GBSCM) approach and is represented as:

$$\gamma_q = P_{ref,q}^{1/2} c_q \left(\frac{d_{ref}}{d_{Tx \rightarrow q} \times d_{q \rightarrow Rx}} \right)^{n_q/2}, \quad (7)$$

where $P_{ref,q}$ is the reference power for the qth DT and n_q is the path-loss exponent. $d_{Tx \rightarrow q}$ and $d_{q \rightarrow Rx}$ represent the distance from Tx to qth DT and qth DT to Rx, respectively. c_q denotes a zero-mean complex Gaussian variable. The delay and Doppler shift of the IDL-DI scatterers can be calculated similarly to the IDL-DTs utilizing (8) and (9) of [15].

2.2.4 Overall Channel Response

The overall channel response is derived by adding the contributions from the individual channel responses:

$$h(t) = h_{DL}(t) + h_{DT}(t) + h_{DI}(t). \quad (8)$$

where h_{DL} , h_{DT} , and h_{DI} denote the DL component, IDL-DTs, and IDL-DI scattering components, respectively.

3 Simulation Setup

This section describes the characteristics of the highway and the distribution of the diffuse scatterers along the highway. Moreover, the traffic flow model and the used simulation tools are also discussed in this section.

3.1.1 Road Layout and Diffuse (DI) Scatterers Distribution

As shown in Fig. 2, for the highway, we consider a 6-lane (3-lanes per direction) highway setup for our simulations. It has a length of 1 km and a width of 27 m in total. The width of each lane is 4.5 m. On both sides of the road, the DI scatterers representing vegetation, scatterers, and points of reflection beyond the road, are considered to model their impact on the overall channel performance. The width of the DI region is $w_{diff} = 5$ m. The distance from the center of the road to the first DI component is $d_{diff} = 17.5$ m. Further, we consider a boundary region of $d_{gap} = 3.75$ m between the start of the DI region and the outermost lanes. The density of the DI scatterers within a given length of one meter is given by x_{diff} . The x and y coordinates of the DI scatterers are modelled by a uniform distribution and are given by:

$$(x_{diff}, y_{diff}) \sim \mathcal{U}\left[(x_{max}, x_{min}), \left(y_{p,diff} \pm \frac{w_{diff}}{2}\right)\right], \quad (9)$$

where $y_{p,diff}$ represents the center of the DI region.

3.1.2 Vehicle Positioning and Trajectory

Vehicles have different starting positions as shown in Fig.2. The Tx and Rx are placed at the opposite ends of the road. Tx and Rx are surrounded by two DTs. The direction of motion of Tx, Rx, and DTs are also given in Fig.2. The vehicles approach each other until the crossover point is reached. At the crossover point the link distance for each vehicle is minimized. Beyond the crossover, as the vehicles continue moving in their respective directions, the link distance increases to its maximum. Since the vehicles have different starting positions and velocities, the crossover occurs at different time instants for each vehicle.

3.1.3 Simulation Tools

For our simulation, we use three mathematical tools.

- For the generation of traffic on the road, we use Simulation of Urban MObility (SUMO), which is an opensource tool used for simulating and analyzing traffic.
- Radiation pattern simulations for the horn and patch antennas were executed using Altair FEKO's Multi-Level Fast Multipole Method (MLFMM) solver at 5.9 GHz frequency.
- Radiation pattern simulations for the phased array Antenna Element (AE) were performed in CST, using the time domain solver at 5.9 GHz. Then, the array radiation patterns were computed using the array factor tool, adjusting the number of elements and phase shifts to obtain the desired configurations.
- MATLAB is used for the signal processing part. Different channel parameters and responses for DL and IDL are calculated. Moreover, received power, excess delay, Doppler shift, trajectory information, and detection capabilities are also evaluated with MATLAB

4 Multiple Antennas for ISAC enabled V2V setup

To enable the use of Multiple Input Multiple Output (MIMO) and antenna diversity techniques, vehicles are designed to incorporate multiple antennas distributed on the surface of their body.

MIMO multiplexing and diversity are well known to enhance data rates and reliability in V2V networks [17]. Therefore, for the accurate modeling of V2V channels, it is important to take into consideration the impact of antenna placement and geometry of cars.

4.1 Antenna Placement Schemes

In our analysis, the placement schemes assumed a Tx equipped with an omnidirectional antenna, while for the Rx radiation patterns with varying directionality were considered.

4.1.1 Front Bumper (FB) Setup

In the front bumper scenario, the Rx is equipped with a directive antenna placed on the front bumper as depicted in Fig.3.

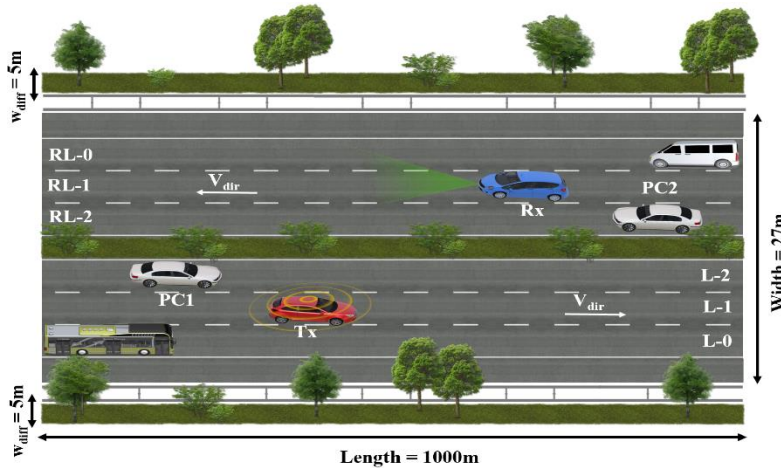


Figure 3. Omnidirectional Tx and front bumper setup

4.1.2 Back Bumper (BB) Setup

In the back bumper scenario, the Rx is equipped with a directive antenna placed on the back bumper as depicted in Fig.4.

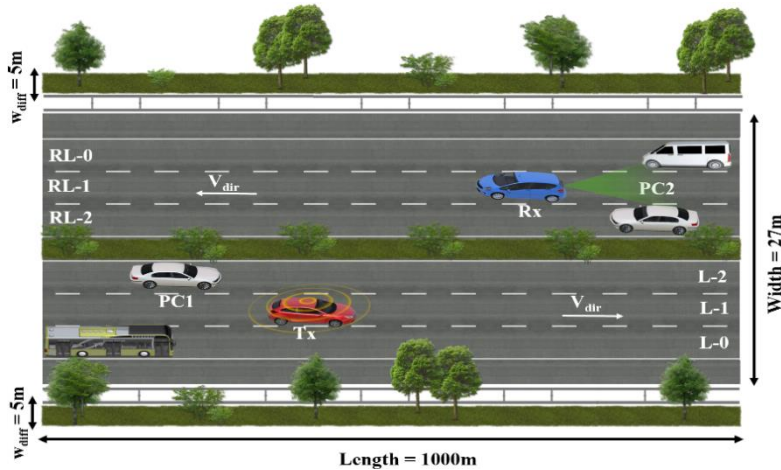


Figure 4. Omnidirectional Tx and back bumper setup

4.1.3 Combined Gain Pattern (CGP) setup

The CGP setup represents the scenario in which the Rx is equipped with identical directive antennas in both the front and back bumpers. We compose the CGP of both antennas by taking the maximum gain value for each angle from both antennas. This can be interpreted as a Selection Combining (SC) diversity scheme, although we consider that, for each time frame, we

can do this SC per angle, which is not completely realistic. Therefore, this could be considered more of an upper bound approach.

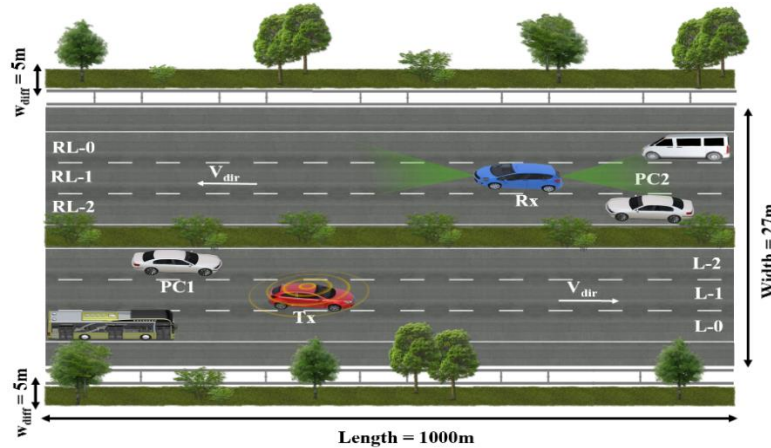


Figure 5. Omnidirectional Tx and CGP setup

4.2 Radiation Patterns

In terms of antenna integration Key Performance Indicators (KPIs) for V2V communication, antennas positioned at the front and back of the vehicle are more advantageous than those on the sides [16]. Therefore, considering the potential for utilizing V2V communication antennas for radar sensing, we analyze the performance of the ISAC-enabled V2V system for the antennas placed at the front and back bumpers of the Rx. Furthermore, the impact of the front and back antennas’ CGP on the overall sensing performance is also assessed. The CGP of the two radiation patterns is computed as:

$$G_{CGP}(\phi) = \max(G_{FB}(\phi), G_{BB}(\phi)), \tag{10}$$

where $G_{FB}(\phi)$ is the gain of the front bumper antenna at azimuth angle ϕ , and $G_{BB}(\phi)$ is the gain of the back bumper antenna at azimuth angle ϕ . Please note that the considered scenario is 2D, and contained in the XY plane, as shown in Fig.6, where the reference coordinate system is presented. The 2D scenario is assumed because V2V communication generally takes place near the horizon, hence only the azimuthal cut at $\theta = 90^\circ$ of the radiation patterns is considered. To assess the impact of different gains on performance, we have utilized both a highly directive antenna (horn) and a less directive antenna (patch) in our analysis. To ensure accuracy, these antennas were integrated into a car model. Specifically, we utilized a simplified hatchback car model to replicate the installed antenna patterns, depicted in Fig.6. This same model was used in [16], [18], [19]. In all cases, the considered working frequency is 5.9 GHz. Note that the symmetry between the patterns is due to the use of a very simplified car model with large flat bumpers, in conjunction with the working frequency, which makes the car and bumpers electrically large compared to the simulated antenna.

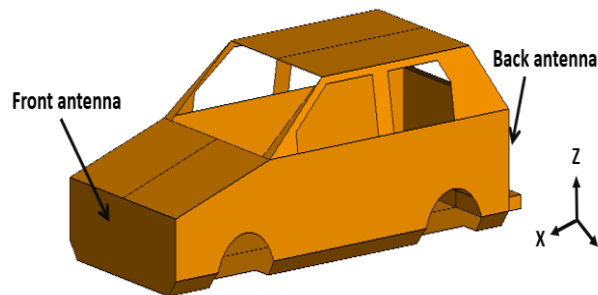


Figure 6. Car model with specified antenna locations

4.2.1 Horn Antenna

Horn antennas are waveguide-based antennas that expand into a flaring section, forming a horn-like shape. This design enhances the directivity and gain of the antenna. Horn antennas are used in vehicular applications due to their high directivity and gain, low loss, and wide beamwidth. Some of the common applications of horn antennas include automotive radars (collision avoidance, blind-spot detection), directional V2V communications, and testing setups for their precision. The gain plots of the horn antenna for front bumper, back bumper, and CGP setup are shown in Fig. 7. It should be noted that a similar behavior takes place in the other hemisphere covering the remaining azimuth angles.

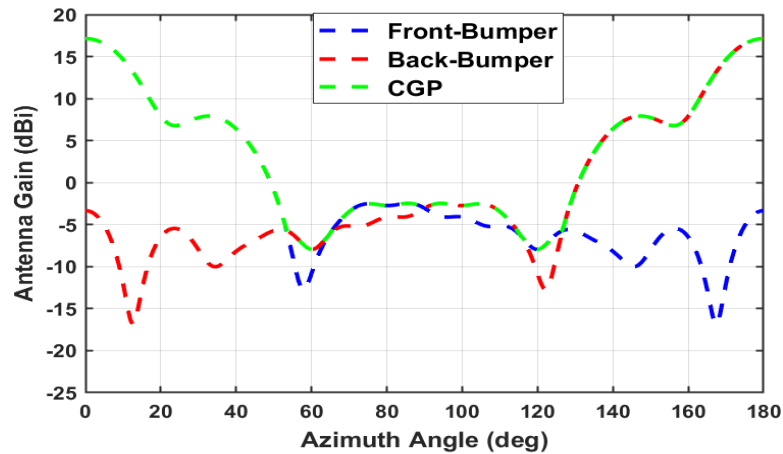


Figure 7. Antenna gain of horn antenna in different setups.

4.2.2 Patch Antenna

Patch antennas are among the most employed antenna types in vehicular applications because of their design and ease of integration, partly due to their flatness. A patch antenna typically consists of a rectangular or circular conductive patch mounted on a grounded dielectric substrate. The electromagnetic waves are radiated perpendicular to the patch which leads to a directional radiation pattern for the patch antenna. Some of the common applications of patch antennas include automotive radars and V2V communications. The gain plots of the patch antenna for front bumper, back bumper, and CGP setup are shown in Fig. 8.

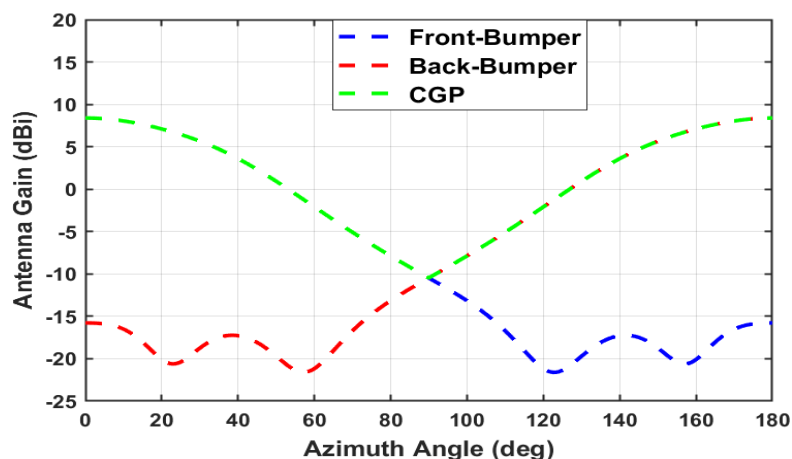


Figure 8. Antenna gain of patch antenna in different setups.

4.2.3 Phased Array Antenna Element

Phased arrays are composed of several AEs. As stated in the previous section, patch antennas are widely used in the automotive industry because of their easy integration. Therefore, phased

arrays made of microstrip patches are commonly used, for both radar and communications. Hence, we use a microstrip patch designed for operation at 5.9 GHz as our phased array AE. In this case, it is simulated in free space. The gain plots of the phased array AE for front bumper, back bumper, and CGP setup are shown in Fig. 9.

To have a fair comparison with the horn and patch antenna, we have used a single AE. The effectiveness of the phased array improves with increasing numbers of AEs (shown in later sections). However, when compared with the patch used integrated into the car model, the phased array AE includes mismatch losses and employs non-ideal, lossy materials, which explains the reduced gain from Fig.9, compared to Fig.8.

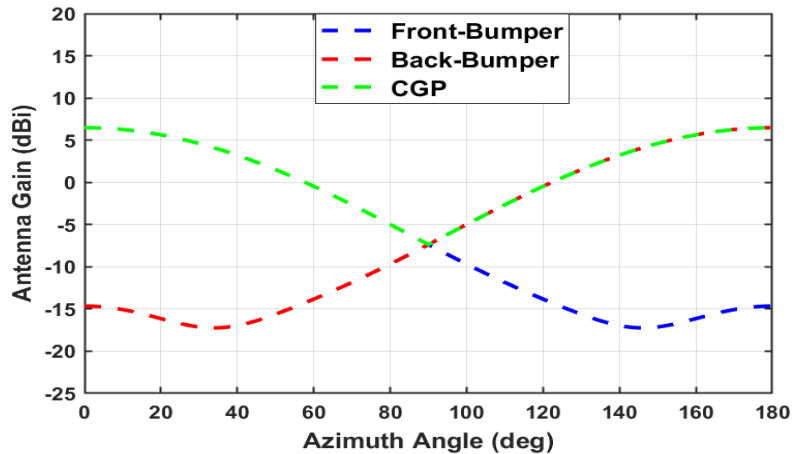


Figure 9. Antenna gain of phased array AE in different setups

4.2.4 Phased Array Configurations

Phased arrays employ multiple AEs which can be controlled individually in phase and, usually, also in amplitude. Not all arrays use identical AEs, such as, for example, in automotive radars, where the tapering for reducing sidelobes is emulated by manipulating the dimensions of each individual AE (see [20], [21] as well as the Franklin antenna array from D1.1, presented in [22]). However, we assume the use of an array where all AEs are identical, and no tapering is applied in any way. The arrays considered are Uniform Linear Arrays (ULAs), with a varying number of either 4, 8, or 16 elements along the azimuthal plane, and an Inter-Element Spacing (IES) of half a wavelength for the design frequency of 5.9 GHz.

Only the single AE is simulated in CST, and then the radiation patterns of the arrays are obtained through the array factor tool, where we also introduce the progressive phase shift to obtain the desired beam scanning direction. The intended scanning directions are within the range of $\pm 60^\circ$, with an angular resolution of either 5° or 10° . Finally, the patterns used for the simulations are the CGP of both phased arrays (front and back bumper) patterns. The phased array patterns are, in turn, combined similarly to the CGP, i.e., for each azimuth angle, the chosen value is the maximum among all the considered beams (be it with 5° or 10° angular resolution). To clarify, the pattern that is considered for the simulations results from the maximum value from each considered beam (be it with 5° or 10° angular resolution) of two identical arrays looking into opposite directions (front bumper and back bumper). This is depicted in Fig. 10. It can be observed that the angular resolution of the scanning has a relevant impact in the pattern for the 16x1 case, being much less relevant for the 8x1 array and almost negligible for the 4x1 array. In addition, the smaller 8x1 and 4x1 arrays experience a much less pronounced drop in the gain towards the 90° , which would be the side of the car. This is all explained by the narrower beamwidth that occurs with a higher count of AEs. However, it has the upside of providing more gain in the front and back directions (towards 0° and 180°) of the car. As stated in [18], within

an automotive context, it makes sense to have more gain towards those directions, so having an increased number of AEs should result in better performance, as it will be shown in this work.

Nevertheless, the way we compose the radiation patterns for the simulations with the arrays is not a very realistic assumption, since it is not technically possible to obtain, at a single time instant, the signal coming from the best possible array and beam at each angle in a phased array. However, simulation time steps are much larger than array switching times, which would also make it unfair to just take a single beam for each array at a snapshot, since it would not necessarily represent the performance of the system, especially in terms of target detection. This assumption is a clear point of future work, being necessary to define a more refined simulation framework that could properly capture aspects such as the array switching times, how often it is needed to detect a target, as well as the scheduling of the ISAC system.

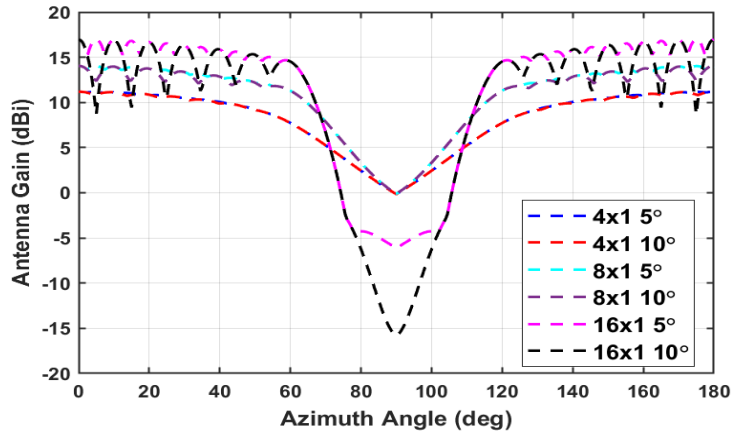


Figure 10. Antenna gain of phased arrays of 4, 8, and 16 AEs, with 5° and 10° beam steering resolution angles

5 Simulation Parameters and Results Discussion

This section discusses the simulation parameters used for our analysis. Additionally, it presents simulation results for horn and patch antennas for all considered setups. We present the simulation results for the aforementioned scenarios at a carrier frequency of $f_c = 5.9$ GHz. We have considered a constant transmitted power value for all the setups to have a fair comparison. The channel magnitude for the DL (h_{DL}) from Tx and IDL from DT (h_{DT}) and DI components (h_{DI}) are calculated and summed at Rx. The rest of the parameters considered along with vehicles' velocity in different lanes are given in Table 1.

Table 1. Simulation Parameters

Parameter	Value
Carrier frequency (f_c)	5.9 GHz
Bandwidth (B)	50 MHz
Transmitted Power	23 dBm
Vehicles' speed in different lanes (L-0, L-1, L-2, RL-0, RL-1, RL-2)	(17, 23, 27, 21, 25, 30) \pm 4 m/s
Simulation Time	25 s
Sample Time	0.01 s
Radar Cross Section (RCS)	10 dBsm
DI Scatterers Density	1 m ⁻²
PL Exponents (DL, DT, DI)	(1.8, 2.0, 5.4)
Horn (P_{ref}) (DL, DT, DI)	(-32.9, -37.7, 62.1) dB
Patch (P_{ref}) (DL, DT, DI)	(-41.7, -46.5, 53.3) dB
Phase (P_{ref}) (DL, DT, DI)	(-43.6, -48.4, 51.4) dB

5.1 Figures of Merit (FoMs)

In traditional communication systems, throughput, latency, and reliability serve as the primary performance evaluation metrics. However, for ISAC systems, additional metrics such as sensing resolution, target detection probability, and accuracy are critical for performance evaluation. In this report, we present channel magnitude/power and target detection results to evaluate the performance of the ISAC-enabled V2V system.

Regarding channel magnitudes, we present

- h_{DL} : channel magnitude of the DL
- h_{DT} : channel magnitude of the DT, comprising the sum of all DTs' channel magnitudes
- h_{DI} : channel magnitude of the DI scatterers
- h : overall channel magnitude, i.e., sum of h_{DL} , h_{DT} , and h_{DI}

The objective of an ISAC system is, among others, to be able to resolve the DTs. For this purpose, it is necessary in the first place to have a backscattered signal from the DTs which is sufficiently above the clutter of the environment, which would be represented here as the DI scatterers signal. Although a more refined threshold for how much that “sufficiently above” is, here we consider that we can clearly distinguish a DT if its channel magnitude is 10 dB over the channel magnitude of the DI scatterers, at a given time instant. Therefore, we define

- Detection Rate (DR) [%]: percentage of time samples where $h_{DT_k} > h_{DI} + 10 \text{ dB}$
 - Defined for individual DTs (Bus, PC1, Van, PC2)
 - Defined also as an average of the DRs of all DTs

Please note that h_{DT_k} is the channel magnitude of the k^{th} DT, which is defined inside the summation from (4). On the other hand, it is also left for future work considering several aspects, such as noise or receiver sensitivity, for which it would be necessary to analyze if the channel magnitude of the different DTs would allow to effectively resolve them, considering also the channel magnitude of the DI scatterers. Another aspect in which DR could be improved is in developing a weighting scheme to target detection, depending on several variables such as the distance to the targets, and their relative speed and direction. Finally, we also present selected target detection snapshots to better illustrate the effects of the different considered antenna setups.

5.2 Horn Antenna

5.2.1 Channel Magnitude of DL, Joint DTs, and DI Scatterers

The channel magnitude curves of DL, joint DTs, and DI scatterers for front bumper, back bumper, and CGP are shown in Fig.11. The joint DTs channel magnitude is calculated by summing the contributions of all the DTs. Similarly, the DI scatterers channel magnitude also results from the summation of contributions from all the scatterers.

The channel magnitude of the front bumper setup is shown in Fig.11(a). The DL is the strongest component, followed by joint DTs and DI scattering components. The DL and joint DTs channel magnitude is high in the first half of the simulation as the main lobe of the Rx is pointing towards the Tx and DTs (Bus, PC1). After the crossover, the main beam points in opposite direction leading to lower values of channel magnitude in the second half of the simulation. The DI scatterers channel magnitude shows a similar behavior. Initially, the number of DI scatterers with higher gain values is higher which is indicated by the higher channel magnitude. As the Rx moves towards the other end of the road, this number decreases, diminishing the channel magnitude of the DI scattering components. As the channel magnitude is higher than the clutter

during the first half only (when the main lobe is aligned), the DL and DTs can be detected only during that time. In case of strong clutter, the DTs will be masked and will not be detected. This highlights the critical importance of beam alignment and environmental dynamics in determining channel performance, emphasizing the need for adaptive strategies to maintain consistent system performance.

Fig.11(b) shows the channel magnitude response of the back bumper setup. The DL is the strongest component, followed by joint DTs and DI scattering components. As the main beam of the Rx does not point to the Tx and DTs (Bus, PC1), lower channel magnitude values are recorded for them in the first half of the simulation. On the other hand, the main beam of the Rx is consistently aligned with the DTs (Van, PC2), resulting in their dominant contribution to the joint DTs channel magnitude. After the crossover, the main beam is directed at the Tx and DTs (Bus, PC1), leading to higher channel magnitude values. The number of DI scatterers with higher gain values is lower in the first half compared to the second half of the simulation. As the antenna is installed at the back bumper, as the Rx moves to the opposite end, the number of DI scatterers with higher gain values also increases. As a result, the channel magnitude of DI scatterers improved in the second half of the simulation. The results imply that link quality in the back bumper setup is suboptimal in the first half of the simulation, leading to significant performance degradation. In the presence of strong clutter, the DTs cannot be detected throughout the simulation.

Similarly, the channel magnitude curves for the CGP setup are displayed in Fig.11(c). In CGP setup, combined radiation pattern of front and back bumper setups is employed. The main lobe of the Rx is always directed at Tx and DTs, except during the crossover interval. The DL is the strongest component throughout the simulation, followed by joint DTs and DI scattering components. During the crossover interval, as the vehicles are parallel to the Rx, the main beam of the Rx does not point to vehicles anymore. As a result, the channel magnitude shows a sharp decline. This impact is visible in Fig.10(c) during $11.5s \leq t_{sim} \leq 13.5s$. However, even after the decline, DL's channel magnitude is still higher than the rest of the components. As the main lobe of the Rx always points to DTs, the corresponding channel magnitude values are also higher. The DI scattering components' channel magnitude shows a symmetric behavior around the crossover point. The d_{bi} around the crossover point is minimum, which results in higher channel magnitude values for the DI scatterers. The results imply that the CGP setup ensures consistently higher channel magnitude throughout the simulation, resulting in improved link quality and target detection, even in the presence of strong clutter during the crossover interval.

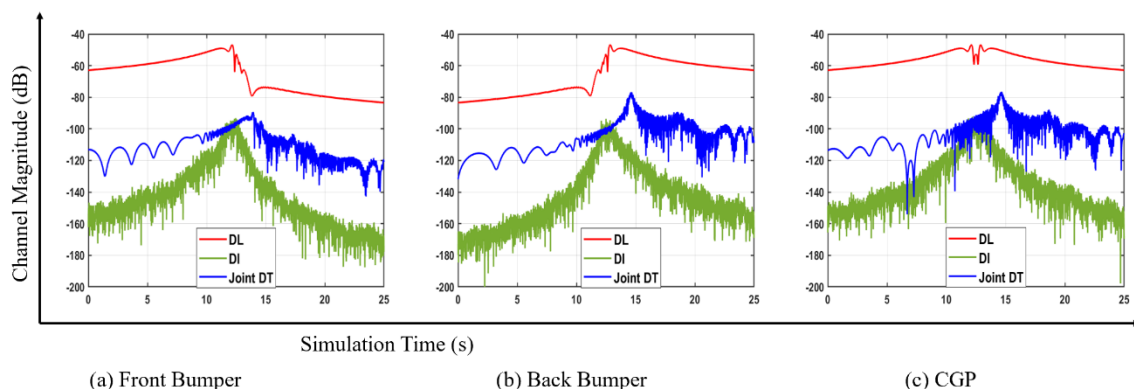


Figure 11. Horn antenna: Channel magnitude of DL, joint DTs, and DI scatterers

5.2.2 Overall Channel Magnitude

The overall channel magnitude for front bumper, back bumper, and CGP setup is shown in Fig.12. The overall channel magnitude is obtained by the summation of contributions from all the components such as DL, IDL-DT, and IDL-DI scatterers.

The overall channel magnitude of the front bumper setup is displayed in Fig.12(a). The overall channel magnitude curve resembles the DL channel magnitude curve as it is the strongest component. For the first half of the simulation, the main beam of the Rx points to the Tx and DTs (Bus, PC1), resulting in higher channel magnitude. After the crossover occurs, the main lobe of the Rx does not point towards Tx and DTs. As a result, the overall channel magnitude is diminished. The fluctuations during the interval of $12s \leq t_{sim} \leq 17s$ comes from the IDL. During this interval, the contributions from IDL-DT and IDL-DI components are highest, resulting in fluctuations in the overall channel magnitude. The front bumper setup experiences a decrease in channel magnitude after the crossover, leading to reduced link quality and potential target detection limitations.

Similarly, Fig.12(b) shows the overall channel magnitude curve of the back bumper setup. The main contributor to the overall channel magnitude is DL, the strongest component. During the first half of the simulation, as the main lobe of the Rx is not aligned with the Tx and DTs (Bus, PC1), the overall channel magnitude is lower. After the crossover, the main lobe points towards the Tx and DTs, resulting in higher overall channel magnitude. The overall channel magnitude curve exhibits fluctuations during the interval of $8s \leq t_{sim} \leq 12.5s$. These fluctuations arise from the IDL-DT and IDL-DI scatterers. During this interval, the IDL contributions are highest. The results indicate that the back bumper setup experiences lower overall channel magnitude during the first half of the simulation, leading to suboptimal link quality and potential detection issues.

Fig.12(c) exhibits the overall channel magnitude curve of the CGP setup. Since the CGP setup utilizes the combined radiation pattern of the front and back bumper configurations, the overall channel magnitude curve remains smooth throughout the simulation. The channel magnitude curve shows a sharp descent during the interval $11s \leq t_{sim} \leq 14s$. This represents the crossover interval of Rx and vehicles. During this interval, the Rx is not oriented toward the vehicles, leading to a descent in the overall channel magnitude. However, during this interval, the contribution from the DL is higher than from IDL, resulting in a minimal impact on the overall channel magnitude in the CGP setup. The CGP setup outperforms the front and back bumper setups in terms of channel magnitude performance. The results suggest that the CGP setup maintains a higher and more stable overall channel magnitude throughout the simulation, ensuring better link quality and more reliable target detection.

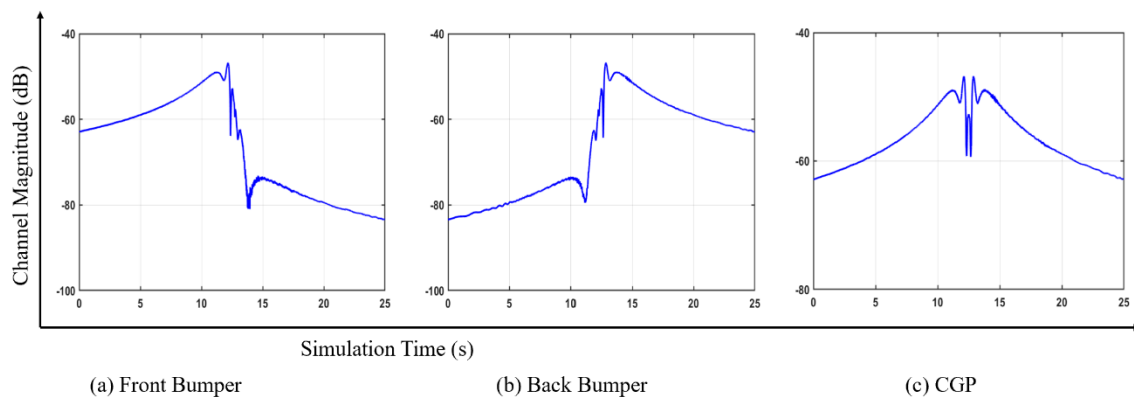


Figure 12. Horn antenna: Overall channel magnitude

5.2.3 Target Detection

The target DR is given in Table 2. It reveals distinct performance characteristics for the front bumper, back bumper, and CGP setups.

The Front Bumper setup achieves high DR for Bus (81.44%) and PC1 (92.84%), as the Rx's main lobe aligns effectively with these targets. However, it struggles significantly with Van (46.64%) and PC2 (58.48%), where alignment is insufficient. This imbalance leads to the lowest average DR of 69.85%, making the front bumper setup the least effective overall.

In contrast, the back bumper setup demonstrates robust performance, with high DR for Van (82.84%) and PC2 (93.6%), thanks to better alignment for Van and PC2. While its performance for Bus (66.6%) is lower than the other setups, its overall average DR of 82.06% indicates consistent and reliable detection.

The CGP setup stands out for its balanced and high DR across all targets, achieving 77% (Bus), 91.6% (PC1), 75.4% (Van), and 88.2% (PC2). With the highest average DR of 83%, it offers superior detection performance by maintaining alignment with all targets throughout the simulation. While it does not outperform the Back Bumper setup for PC2 and Van individually, its consistency across all targets makes it the most versatile and reliable solution. Thus, CGP setup is optimal for achieving balanced detection in diverse scenarios.

Table 2. DT detection rate for horn antenna setup

Detection Rate (DR)	Bus	PC1	Van	PC2	Average DR
Front Bumper	81.44	92.84	46.64	58.48	69.85
Back Bumper	66.6	85.2	82.84	93.6	82.06
CGP	77	91.6	75.4	88.2	83

As mentioned previously, target detection is carried out continuously throughout the simulation. The selected snapshot time instances (12s and 14s) are chosen based on the condition that the received power of all components is sufficiently high, ensuring their visibility in the snapshots. It is important to highlight that we have not selected these time instants to offer optimal performance, but rather to demonstrate the behavior and trends at specific points during the simulation, without implying that these are the points of best performance. These time instances capture the system's behavior both before and after the Rx passes the Tx, offering insights into the system's performance across different stages of the simulation.

The presented snapshots align well with the DR data and offer valuable insight into the detection of the DL from the Tx. The snapshots demonstrate how the alignment of the Rx's main lobe with the Tx and DTs directly influences detection accuracy. High DR values for targets like PC1 and Bus in the front bumper setup are reflected in the snapshots, where strong signal power enables clear detection. Similarly, the back bumper setup's superior performance for targets like Van and PC2 corresponds to its favorable main lobe orientation in the snapshots. The CGP setup's balanced detection across all targets is evident in its snapshots, highlighting consistent DL detection and robust performance for both direct and indirect targets. These visualizations corroborate the DR results and emphasize the importance of optimal Rx alignment for effective target detection.

The target detection snapshot at $t_{sim} = 12s$ suggests that the CGP setup offers superior target detection capabilities, as it combines the advantages of both the front and back bumper setups, providing higher power levels for all DTs and ensuring better detection, even in the presence of clutter, compared to the individual bumper setups.

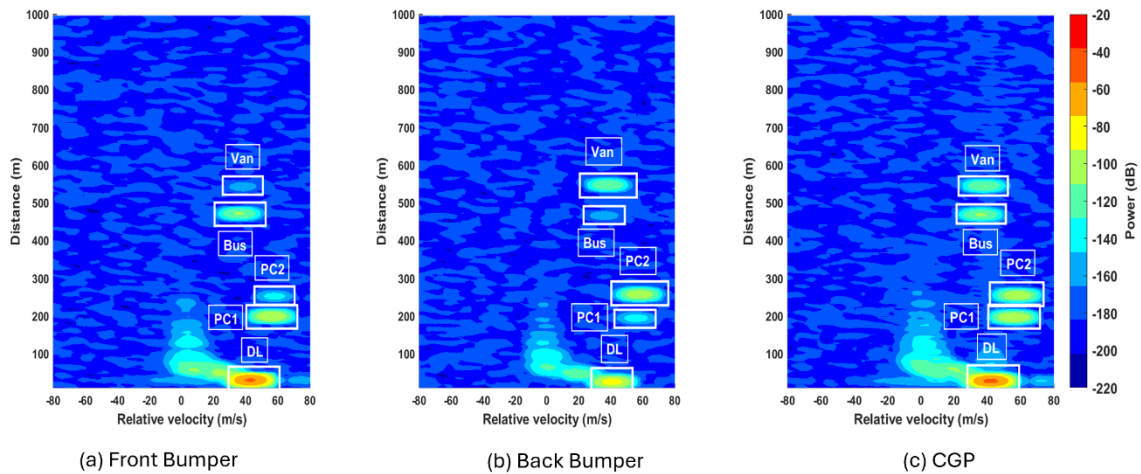


Figure 13. Horn antenna: Target detection snapshot at 12s

Similarly, the snapshot at $t_{sim} = 14s$ highlight that the CGP setup consistently outperforms the front and back bumper setups in terms of target detection, as it maintains higher power levels for all DTs throughout the simulation, ensuring better detection capability even after the crossover and in the presence of strong clutter. This makes the CGP setup more reliable for accurate target detection across varying conditions.

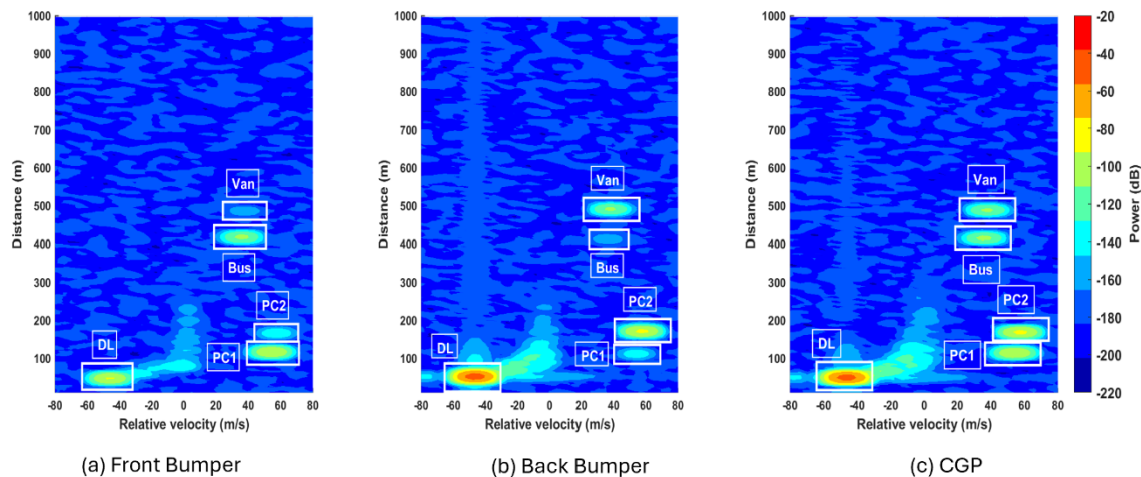


Figure 14. Horn antenna: Target detection snapshot at 14s

5.3 Patch Antenna

5.3.1 Channel Magnitude of DL, Joint DTs, and DI Scatterers

The channel magnitude of patch antenna for different antenna placement setups are illustrated in Fig.15. The channel magnitude curves for the front bumper setup are shown in Fig.15(a). As the main lobe of the Rx is directed at the Tx for the first half of the simulation, higher channel magnitude values are recorded for the DL. After the crossover, the channel magnitude values are diminished as the main lobe of the Rx does not point to the Tx anymore. Similarly, the joint DTs channel magnitude is also higher in the first half because the main lobe of the Rx is directed at DTs (Bus, PC1). As a result, the channel magnitude of Bus and PC1 is higher. As a result, the joint DTs channel magnitude is also higher. The number of DI scatterers with high gain values is greater in the first half compared to the second half of the simulation. As a result, the channel magnitude of DI scattering components is higher in the first half of the simulation. The link quality in the front bumper setup is optimal in the first half of the simulation when the Rx is aligned with the Tx and DTs, leading to higher channel magnitudes. However, after the

crossover, the channel magnitude decreases, potentially affecting target detection and system performance. This highlights the importance of antenna alignment for maintaining strong link quality throughout the simulation.

Similarly, the channel magnitude of the back bumper setup is shown in Fig.15(b). The DL is the strongest component, followed by joint DTs and DI scattering components. The main lobe of the Rx does not point to the Tx and DTs (Bus, PC1) for the first half of the simulation, leading to lower channel magnitude values. After the crossover, the main beam is aligned with the Tx and the DTs (Bus, PC1), leading to higher channel magnitude values. As a result, higher channel magnitude values are recorded for the DL and joint DTs in the second half of the simulation. For DI scattering components, the channel magnitude also exhibits similar behavior. The number of DI scatterers with high gain values is lower in the first half compared to the second half of the simulation. This leads to higher channel magnitude for DI scatterers in the second half of the simulation. The back bumper setup experiences lower link quality in the first half of the simulation when the Rx is not aligned with the Tx and DTs, resulting in lower channel magnitudes. This reduces the performance and target detection capabilities of the ISAC-enabled V2V system. After the crossover, the alignment of the Rx improves, causing an increase in channel magnitudes, which leads to a notable enhancement in link quality and better target detection performance.

The channel magnitude response for the CGP setup is shown in Fig.15(c). As combined radiation patterns are employed, the channel magnitude performance is better than front and back bumper setups. As the main lobe of the Rx points to the Tx and DTs throughout the simulation, except the crossover interval, leading to higher channel magnitudes. During the crossover interval, the channel magnitude of the DL shows a sharp descent. This sharp descent is because the Tx and Rx are parallel to each other and the main lobe of the Rx does not point to Tx during the crossover interval. A similar type of sharp descent is also observed in the channel magnitude of DTs (Bus, PC1) as they cross Rx. This type of behavior is not recorded in the channel magnitude of DTs (Van, PC2), as they never cross Rx. The CGP setup ensures higher channel magnitudes throughout most of the simulation, contributing to improved link quality and target detection. However, the sharp decline in channel magnitude during the crossover interval may impact detection accuracy temporarily, highlighting the need for continuous alignment during critical periods.

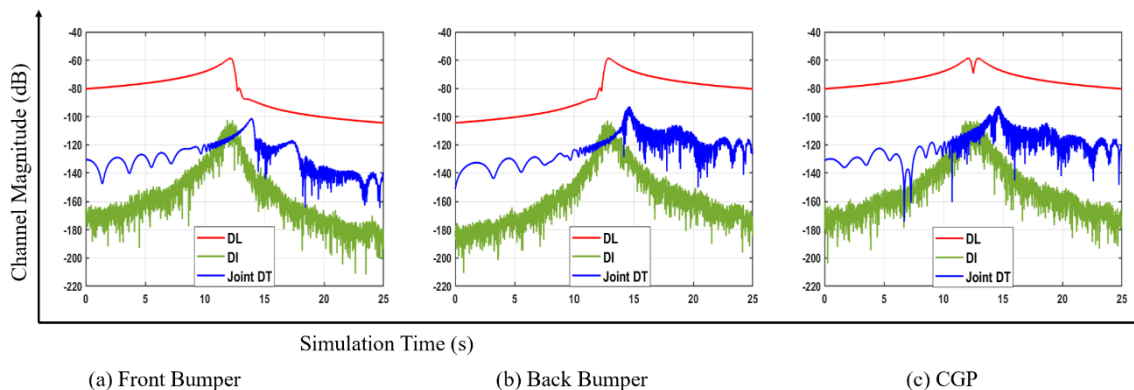


Figure 15. Patch antenna: Channel magnitude of DL, joint DTs, and DI scatterers

5.3.2 Overall Channel Magnitude

The overall channel magnitude curves of the patch antenna for different antenna placement setups are displayed in Fig.16. The overall channel magnitude represents the summation of all the components i.e., DL, DTs, and DI scattering components.

The overall channel magnitude for the front bumper setup is shown in Fig.16(a). The overall channel magnitude curve resembles DL as it is the strongest component of all. For the first half of the simulation, higher values of channel magnitude are recorded as main lobe of the Rx points to the Tx and DTs (Bus, PC1). After the crossover, the channel magnitude values diminish as the main lobe of the Rx is not directed towards Tx and DTs (Bus, PC1). The variations in the overall channel magnitude during the interval $12.5s \leq t_{sim} \leq 17.5s$ are due to the DTs and DI scattering components. During this interval, the contribution from the IDL is the strongest which is visible in the overall channel magnitude. The front bumper setup exhibits higher overall channel magnitude values during the first half of the simulation, ensuring better link quality and target detection capability. However, after the crossover, the diminished alignment leads to lower channel magnitudes, which impacts the target detection capability.

Similarly, the overall channel magnitude for the back bumper setup is given in Fig.16(b). The channel magnitude response is opposite to the front bumper setup as the antenna is installed at the back bumper. The channel magnitude is lower in the first half because the main lobe of the Rx is not aligned with the Tx and DTs (Bus, PC1). After the crossover, the main beam of the Rx is directed at the Tx and DTs, leading to higher values of the channel magnitude. The variations in the overall channel magnitude are recorded during the interval $10s \leq t_{sim} \leq 12.5s$. As the main lobe of the Rx is not directed at the Tx and DTs during this interval, the contribution from the IDL-DTs and IDL-DI components become stronger indicated by the fluctuations in the overall channel magnitude. The back bumper setup experiences suboptimal channel magnitude in the first half of the simulation due to misalignment, leading to potential challenges in target detection. However, after the crossover, improved alignment enhances channel magnitude, resulting in better link quality and target detection capability.

The overall channel magnitude for the CGP setup is shown in Fig.16(c). The main lobe of the Rx is always directed at Tx and DTs. As a result, higher channel magnitude values are recorded throughout the simulation, except during the crossover interval. During the crossover interval, vehicles are parallel to Rx and the main lobe is not directed at them, leading to sharp descent in the channel magnitude values. As the main lobe of the Rx is always directed at the Tx, the DL is always the strongest component. There are no visible variations due to the IDL-DTs and IDL-DI components. The results indicate that the CGP setup provides consistently high channel magnitude values throughout most of the simulation. This behavior highlights the CGP setup's ability to maintain superior target detection accuracy and link stability compared to other antenna placement setups.

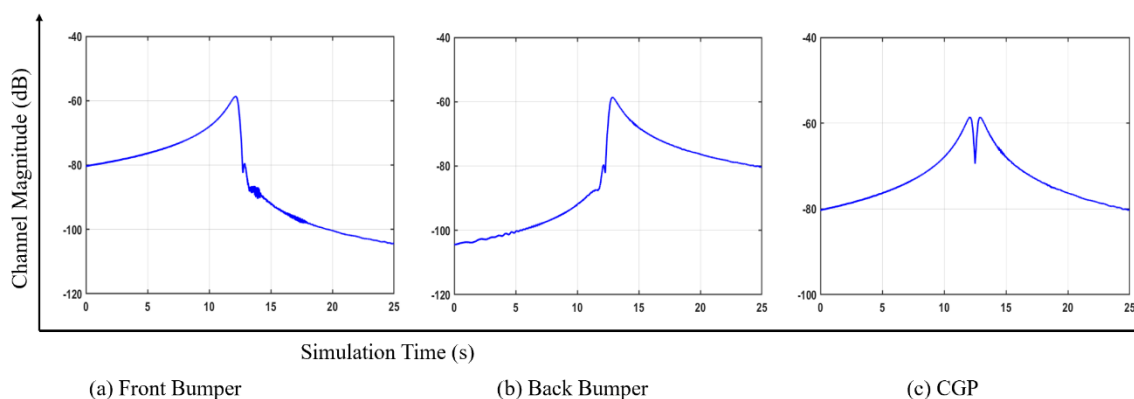


Figure 16. Patch antenna: Overall channel magnitude

5.3.3 Target Detection

The DR data highlights distinct performance characteristics for each antenna placement setup. The front bumper setup demonstrates a strong detection rate for forward-facing targets like Bus (79.96%) and PC1 (89%), as the Rx's main lobe is aligned with these targets in the first half of the simulation. However, its performance for DT Van (38.12%) and PC2 (50.64%) is significantly lower, which reduces the overall average DR to 64.43%.

The back bumper setup excels in detecting and achieving high DR values for Van (80.16%) and PC2 (90.92%), as its main lobe remains directed at these targets throughout the simulation. Its performance for forward-facing targets, however, is weaker, with lower DR values for Bus (56.48%) and PC1 (77.12%). Despite this, the back bumper setup achieves an average DR of 76.17%, indicating better overall detection than the front bumper.

The CGP setup offers the most balanced performance, with consistently high DR values across all targets. It achieves 74.96% for Bus, 88.04% for PC1, 72.64% for Van, and 84.32% for PC2. This balanced detection capability results in the highest average DR of 79.99%, showcasing its superiority in maintaining consistent detection accuracy for both forward and rearward targets. Overall, the CGP setup outperforms the other configurations in terms of average DR and versatility across all target types.

Table 3. DT detection rate for patch antenna setup

Detection Rate (DR)	Bus	PC1	Van	PC2	Average DR
Front Bumper	79.96	89	38.12	50.64	64.43
Back Bumper	56.48	77.12	80.16	90.92	76.17
CGP	74.96	88.04	72.64	84.32	79.99

The target detection snapshots for all setups using a patch antenna illustrate similar phenomena. These snapshots clearly demonstrate how the detection performance varies based on the alignment of the Rx's main lobe with the targets. For the Front Bumper setup, forward-facing targets (Bus and PC1) exhibit strong detection, while rearward targets (Van and PC2) show reduced detection due to insufficient power levels. In contrast, the Back Bumper setup excels in detecting rearward targets but struggles with forward-facing ones. The CGP setup consistently shows superior detection for all targets, aligning well with the observed DR values and confirming its balanced and robust performance across varying scenarios.

The target detection snapshot at $t_{sim} = 12s$ imply that the CGP setup provides superior target detection accuracy compared to the front and back bumper setups due to its consistent alignment of Rx with the Tx and DTs, resulting in higher power levels for all targets. In contrast, the front bumper setup struggles to detect some targets (Van, PC2) at certain times due to insufficient power, while the back bumper setup has difficulty detecting Bus and PC1 but can reliably detect Van and PC2. This highlights that the CGP setup offers a more reliable and efficient detection capability across the entire simulation.

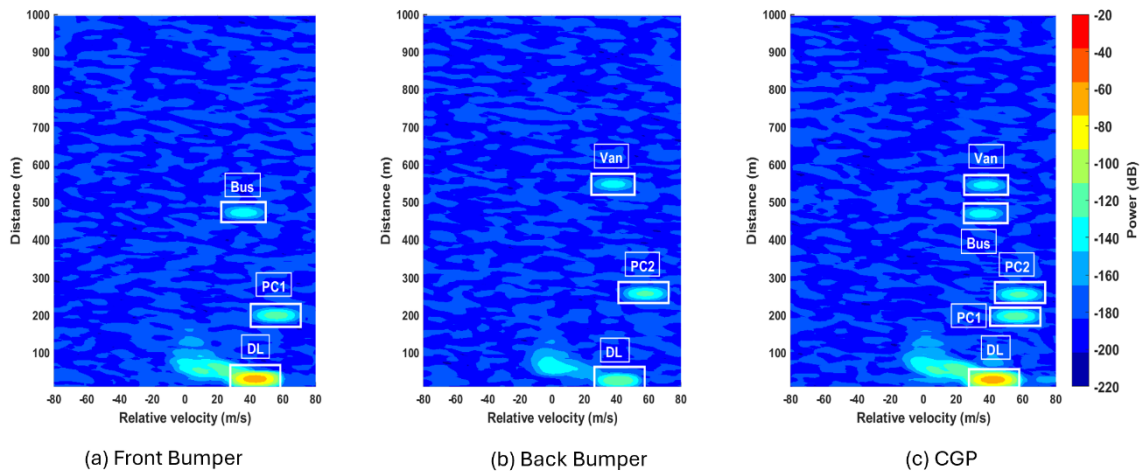


Figure 17. Patch antenna: Target detection snapshot at 12s

In the same way, the target detection snapshot at $t_{sim} = 14s$ indicates that the CGP setup significantly enhances target detection capability compared to the front and back bumper setups. By maintaining consistent alignment with the Tx and DTs throughout the simulation, the CGP setup ensures higher power levels for all components, facilitating reliable detection of both DL and DTs. In contrast, the front and back bumper setups suffer from reduced target detection capability due to misalignment during certain intervals, resulting in undetected DTs. Thus, the CGP setup offers a more robust and reliable solution for ISAC-enabled V2V systems, ensuring continuous target detection across a wider range of scenarios.

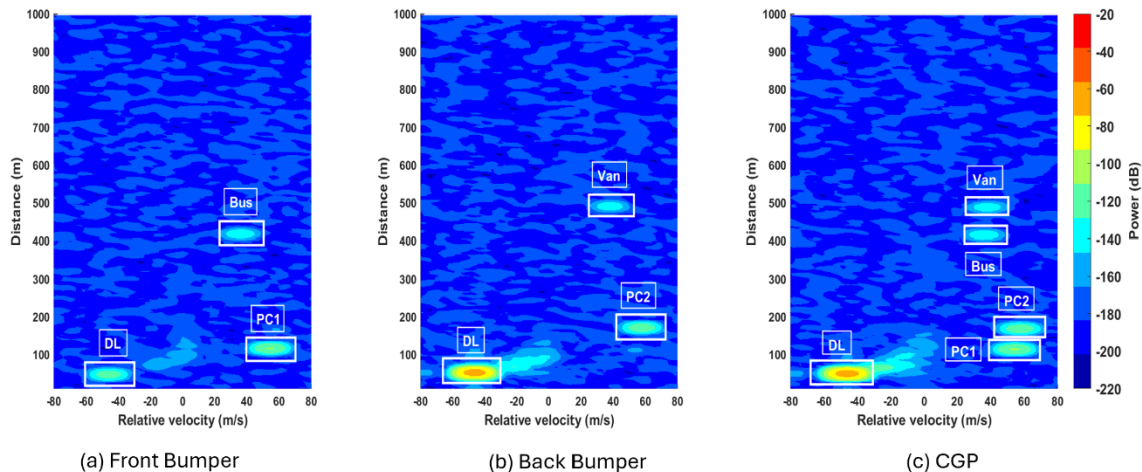


Figure 18. Patch antenna: Target detection snapshot at 14s

5.4 Phased Array Antenna Element

5.4.1 Channel Magnitude of DL, Joint DTs, and DI Scatterers

The channel magnitude curves of the phased array AE for all the antenna placement setups are given in Fig.19. The channel magnitude for the front bumper setup is shown in Fig.19(a). The DL is the strongest component, followed by joint DTs and DI scattering components. During the first half the simulation, the main lobe of the Rx is directed at the Tx and DTs (Bus, PC1). As a result, higher channel magnitude values are recorded for the DL and joint DTs. After the crossover occurs, the Rx’s main lobe is not directed at Tx and DTs, leading to a decrease in the channel magnitude. The channel magnitude of the DI scattering components is also elevated in the first half, owing to the larger number of DI scatterers with higher gain values. As the Rx moves to the other end of the road, this number decreases, resulting in a decrease in the channel magnitude.

The front bumper setup shows a decrease in channel magnitude after the crossover due to misalignment of the Rx's main lobe with the Tx and DTs. This results in reduced detection capabilities and a decline in link quality, emphasizing the importance of antenna alignment for maintaining consistent performance.

Similarly, Fig.19(b) exhibits the channel magnitude of the back bumper setup. The channel magnitude response is opposite to the front bumper. The channel magnitude of the DL and joint DTs is low in the first half because the main lobe of the Rx does not point at them. After the crossover, the main lobe aligns with the Tx and DTs, which causes the channel magnitude to improve in the second half of the simulation. A similar behavior is observed in the channel magnitude of DI scattering components. The back bumper setup shows a shift in channel magnitude after the crossover, with a low channel magnitude during the first half as the Rx's main lobe is not aligned with the Tx and DTs. However, after the crossover, alignment improves, resulting in a significant increase in channel magnitude and improved detection performance in the second half of the simulation.

The channel magnitude of the CGP setup of the phase antenna is shown in Fig.19(c). The DL is the strongest component, followed by DTs and DI scattering components. The main lobe of the Rx is always directed at the Tx and DTs, except during the crossover interval. As a result, the channel magnitude of the DL and DTs is always higher than the front and back bumper setups. The channel magnitude of the DI scattering components exhibits a symmetric behavior around the crossover point. As Tx and Rx approach each other, the d_{bi} decreases resulting in an increase in the channel magnitude of the DI scattering components. After the crossover, as Tx and Rx move away from one another, d_{bi} increases leading to a decrease in the channel magnitude of the DI scattering components. The CGP setup provides consistently higher channel magnitudes throughout most of the simulation, which leads to improved target detection capability. The stable alignment of the main lobe ensures that the DTs are consistently detectable. In contrast, the front and back bumper setups results in less reliable target detection performance, especially when the Rx is misaligned with the Tx and DTs. The CGP setup's superior channel magnitude performance enhances target detection capability, making it more suitable for ISAC-enabled V2V systems.

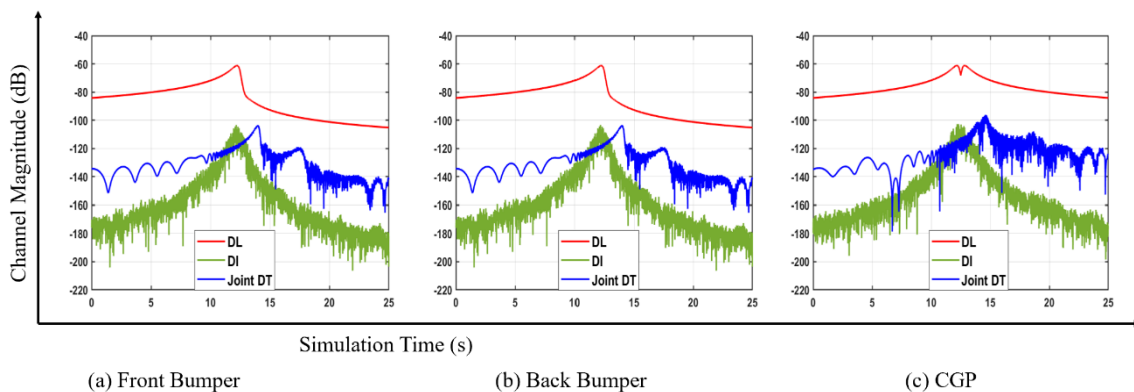


Figure 19. Phased array AE: Channel magnitude of DL, joint DTs, and DI scatterers

5.4.2 Overall Channel Magnitude

The overall channel magnitude of the phase antenna for different antenna placement schemes is showing in Fig.20. The overall channel magnitude represents the summation of all the components such as DL, DTs, and DI scattering components. The overall channel magnitude of the front bumper setup is displayed in Fig.20(a). In the first half of the simulation, the main lobe of the Rx is directed at the Tx and DTs (Bus, PC1) resulting in higher contributions from them in the overall channel magnitude. After the crossover, the overall channel magnitude is decreased

as the main is not directed at Tx and DTs anymore. The variations in the overall channel magnitude during the interval $13s \leq t_{sim} \leq 18s$ arise from the IDL-DTs and IDL-DI scattering components. During this interval, the contribution from the DL is weaker than the IDL. The decrease in overall channel magnitude after the crossover in the front bumper setup leads to reduced target detection capability, as the Rx no longer aligns with the Tx and DTs, weakening the detection of these targets. This emphasizes the need for continuous alignment for optimal detection in V2V systems.

Fig.20(b) shows the overall channel magnitude curve of the back bumper setup. The channel magnitude is lower in the first half of the simulation because the main lobe of the Rx is not aligned with the Tx and DTs. After the crossover, the main lobe of the Rx is directed at the Tx and DTs, resulting in higher channel magnitude. The variations in the overall channel magnitude curve during the interval $9s \leq t_{sim} \leq 13s$ are due to the IDL-DT and IDL-DI scattering components. The decrease in overall channel magnitude in the first half of the simulation for the back bumper setup, due to the misalignment of the Rx with the Tx and DTs, leads to lower channel magnitude performance and target detection capability.

The overall channel magnitude curve of the CGP setup is given in Fig.20(c). The overall channel magnitude in the CGP setup is higher through the simulation, except during the crossover interval. During the crossover interval, the Rx is parallel to the vehicles, and the main lobe of the Rx is not directed at the vehicles. As a result, the channel magnitude is diminished. Other than the crossover interval, the channel magnitude performance of the CGP setup is better than the front and back bumper setups. It results in higher overall channel magnitude performance throughout the simulation. The higher overall channel magnitude of the CGP setup throughout the simulation, except during the crossover interval, indicates superior target detection capability compared to the front and back bumper setups. The sharp decrease during the crossover interval, when the Rx is parallel to the vehicles, highlights a temporary reduction in detection accuracy. However, outside of this period, the consistent and higher channel magnitude performance of the CGP setup ensures enhanced detection reliability and overall performance.

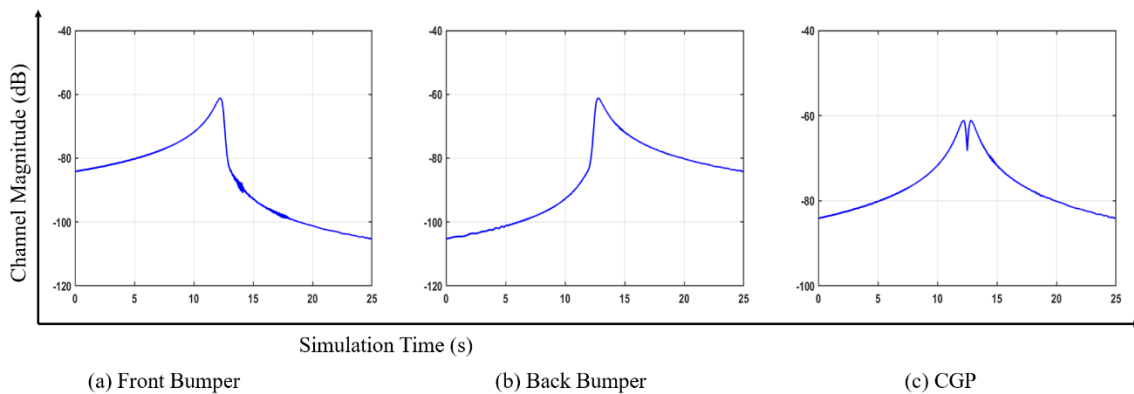


Figure 20. Phased array AE: Overall channel magnitude

5.4.3 Target Detection

The DR data highlights the strengths and limitations of the three antenna setups in detecting different targets: Bus, PC1, Van, and PC2. The DR data for the patch antenna is provided in Table 4. The front bumper setup demonstrates high detection rates for the Bus (78.88%) and PC1 (88.6%), as the main lobe of the Rx is aligned with forward-facing targets. However, the detection rates for the Van (41.12%) and PC2 (54.76%) are notably lower due to insufficient power levels from the targets located at the backside of the Rx. This leads to the lowest average DR of 65.84% among the setups.

The back bumper configuration excels in detecting rearward targets, with detection rates of 79.12% for the Van and 89.24% for PC2. However, forward-facing targets such as the Bus (57.6%) and PC1 (77.96%) have reduced detection rates due to the alignment of the main lobe. The average DR improves to 75.98%, reflecting its better overall performance compared to the front bumper setup.

The CGP setup achieves a balanced performance across all targets, with detection rates of 75.04% for the Bus, 87.56% for PC1, 72.32% for the Van, and 83.52% for PC2. This setup benefits from its combined radiation pattern, which ensures consistent alignment with the Tx and DTs. As a result, the CGP setup achieves the highest average DR of 79.61%, demonstrating superior detection capability and overall robustness.

Table 4. DT detection for phased array AE

Detection Rate (DR)	Bus	PC1	Van	PC2	Average DR
Front Bumper	78.88	88.6	41.12	54.76	65.84
Back Bumper	57.6	77.96	79.12	89.24	75.98
CGP	75.04	87.56	72.32	83.52	79.61

The target detection snapshots illustrate a similar behavior, reinforcing the detection patterns observed in the detection rate data. They highlight the strengths and limitations of each antenna placement setup, providing a visual representation of the varying detection capabilities across different targets.

The target detection snapshot at $t_{sim} = 12s$ highlights that the CGP setup provides superior target detection capability compared to the front and back bumper setups. The constant alignment of the Rx's main lobe with the Tx and DTs in the CGP setup ensures consistently higher power levels, making it easier to distinguish targets from the clutter. In contrast, the front and back bumper setups experience detection limitations due to suboptimal alignment, leading to lower power levels and reduced target detection capabilities, particularly for certain DTs (Van, PC2) and DTs (Bus, PC1). The use of a combined radiation pattern in the CGP setup improves the system's overall detection performance, enhancing its reliability for identifying targets.

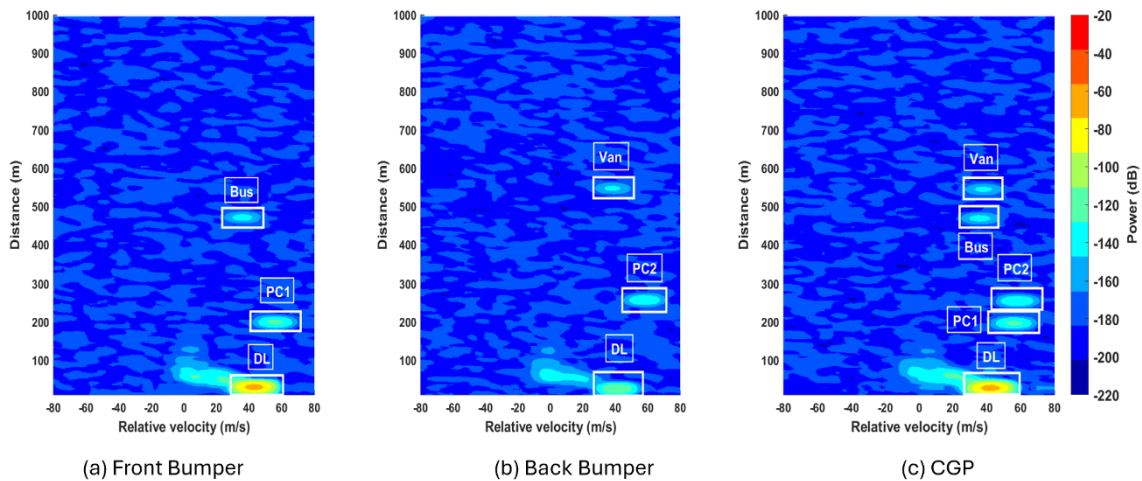


Figure 21. Phased array AE: Target detection snapshot at 12s

Similarly, the target detection snapshot at $t_{sim} = 14s$ highlights that CGP setup consistently provides higher power levels across all targets, leading to better detection accuracy compared to the front and back bumper setups. In the front bumper setup, the power levels of DTs (Van, PC2) are insufficient for detection, while DTs (Bus, PC1) can be easily detected due to higher power levels. In the back bumper setup, the power levels of DTs (Van, PC2) are higher, allowing

for successful detection, while DTs (Bus, PC1) go undetected. The CGP setup ensures that all vehicles, including the Tx and DTs, are detected throughout the simulation, offering superior performance in target detection and identification.

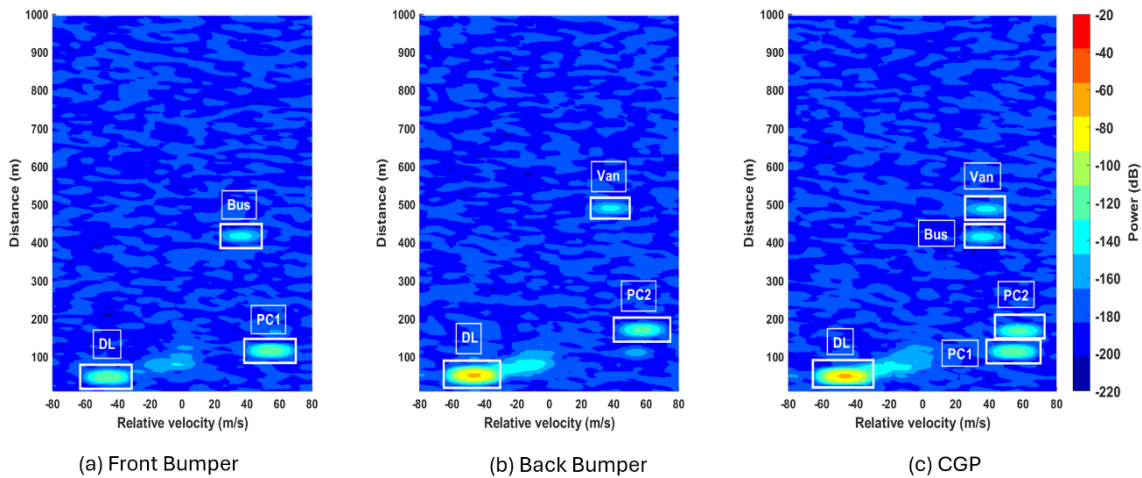


Figure 22. Phased array AE: Target detection snapshot at 14s

5.5 Statistical Characteristics of Different Placement Schemes

The statistical properties of various antenna radiation patterns and placement schemes are summarized in Table 5. These properties offer insights into the average channel magnitude for the different configurations. Table 5 also includes the coefficient of variation, which quantifies the variation of the channel magnitude relative to its mean value, providing a measure of consistency across setups. In addition, Table 5 shows the average DR for each of the considered cases.

The average channel magnitude of the DL is the same for the front and back bumper setups across different configurations. This is expected due to the symmetric placement of the cars involved in the DL. On the other hand, the DL of the CGP setup achieves around 5dB gain compared to the front and back bumper setups, which would lead to a superior performance in terms of data rate or energy consumption for the DL. For joint DTs, the back bumper setup demonstrates better performance compared to the front bumper setup. This performance difference is attributed to the vehicles' trajectories, including their relative distance from the Rx and the distance covered within the simulation time. The maximum differences of 7.4dB, 6dB, and 5dB are observed in the case of the horn, patch, and phased array AE, respectively. Nonetheless, the joint channel magnitude of the CGP setup consistently surpasses that of the front and back bumper setups across all configurations. Similarly, the average channel magnitude of DI scatterers is almost identical in the front and back bumper setups for all the configurations. However, the CGP setup yields the highest average channel magnitude of DI scatterers. A difference of approximately 3.5 dB is observed for all the setups. It is worth noting that, while the DI scatterers might be useful for the communications part, they are not desirable for the sensing functions, since they represent clutter that could mask the DTs. However, the magnitude of the joint DTs is still generally larger than the DI scatterers, which is showcased in the DR, although, on average, the ratio between joint DTs and DI scatterers decreases in the CGP cases.

Going into detail with target DR, we can see that there is an improvement when using the horn antenna over the patch antenna or the phased array AE, which both perform similarly in all cases. The front bumper cases underperform poorly. Finally, the CGP setups, looking just at the

average target DR, seem to provide just a slight enhancement when compared to back bumper setups. However, this average target DR is not capturing the fact that, for back bumper setups, two of the DTs (Bus and PC1) have lower or much lower DR than for the CGP setups. However, the average DR is not so different between the back bumper and CGP setups due to the other two DTs (Van and PC2) having larger DR. This is due to the single antenna (back/front bumper) capturing less power coming from the DI scatterers. On the other hand, this reveals that the CGP setups are better than the back bumper setups also in terms of “fairness”, which is a common aspect analyzed for communication systems.

The horn antenna setup results in the highest channel magnitude, followed by the patch and phased array AE antenna setup as given in Table 2. For the DL, a difference of 15.3dB is observed for the horn and patch antenna setups. Similarly, for joint DTs, a difference of 15.5dB, 17.08dB, and 16.57dB is noted among the front bumper, back bumper, and CGP setups, respectively. Regarding DI scatterers, the horn antenna setup delivers a channel magnitude which is approximately 11.5dB higher than that of the patch antenna setup.

The patch antenna setup demonstrates superior channel magnitude performance compared to the phased array AE setup. This is mainly explained by the consideration of mismatch losses and non-ideal, lossy materials for the phased array AE. For DL and joint DTs, the patch antenna delivers a channel magnitude that is 3.5dB higher than the phased array AE setup across all placement schemes. For DI scatterers, the channel magnitude of the records a 1.7dB improvement in all the placement schemes.

Table 5. Statistical properties of different placement schemes

Type	Setup	Mean (dB)			Coefficient of Variation			Average DR
		DL	IDL-DTs	IDL-DI	DL	IDL-DTs	IDL-DI	
Horn	F-B	-60.67	-107.03	-121.62	1.08	1.2	2.99	69.85
	B-B	-60.67	-99.63	-122.55	1.08	1.66	2.87	82.06
	CGP	-55.55	-98.31	-119.28	0.55	1.48	2.53	83
Patch	F-B	-76.31	-122.57	-133.68	1.45	1.64	3.25	64.43
	B-B	-76.31	-116.71	-133.93	1.45	1.78	3.24	76.17
	CGP	-70.88	-114.88	-130.17	0.88	1.58	2.81	79.99
Phase	F-B	-79.43	-125.53	-135.39	1.48	1.7	3.4	65.84
	B-B	-79.43	-120.37	-135.39	1.48	1.81	3.32	75.98
	CGP	-74.27	-118.44	-131.9	0.96	1.6	3.01	79.61

*Coefficient of Variation = $\frac{\hat{\sigma}}{\hat{\mu}}$, where $\hat{\sigma}$ and $\hat{\mu}$ represent standard deviation and mean estimates, respectively.

*F-B represents Front Bumper Setup

* B-B represents Back Bumper Setup

The CGP setup consistently delivers superior performance in terms of channel magnitude for DL, joint DTs, and DI scatterers compared to front and back bumper setups. The horn antenna setup yields the highest channel magnitude, followed by the patch and phased array AE setups, with differences as high as 15.5dB for the DL, 17dB for joint DTs, and 11.5dB for DI scatterers. The patch antenna outperforms the phase AE setup, providing higher channel magnitude across all configurations, particularly in DL and DI scatterers, with differences of up to 3.5dB and 1.7dB, respectively. These variations highlight the impact of antenna type and placement on system performance.

On the other hand, CGP setups not only provide an increased average value of all considered magnitudes (DL, joint DTs and DI scatterers), but also yield a lower coefficient of variation, which implies smaller relative variations compared to their means. In addition, we observe a decreasing coefficient of variation with an increase in average values, following the order horn antenna, patch antenna, and phased array AE.

Moreover, the increase of joint DTs magnitude is larger than the increase of DI scatterers magnitude when going from the phased array AE, to then the patch antenna and, as the best case, the horn antenna. In other words, the clutter level (DI scatterers magnitude) increases less than the useful DTs magnitudes, which should lead to better sensing performance. Taking this into account, we can affirm that there is an undoubtedly better performance (horn-best, patch-middle, phased array AE-worst), since not only the average magnitudes increase, but also the relative variation decreases, which implies that, e.g., going below a certain threshold of DL or DT magnitude is less likely to happen, on top of having a larger average magnitude, that, in the case of DL, could be used, for example, to achieve higher data rates.

5.6 Phased Arrays

Phased arrays for performance evaluation on the road are presented in this section. As described previously, we have employed different ULA configurations, with either 4, 8, or 18 elements, as well as a beam steering resolution of 5° and 10° of the intended scanning direction. In this section, we will compare the performance of the different considered phased arrays in terms of channel magnitude and target detection accuracy. For this purpose, we have assumed a CGP setup where a combined radiation pattern of the front and back bumper setups is utilized, combining in the same way the patterns for each beamforming state of both arrays. The Tx is still assumed to be omnidirectional. Both back and front arrays are identical.

5.6.1 Channel Magnitude of DL, Joint DTs, and DI Scatterers

The channel magnitude of DL, joint DTs, and DI scattering components of systems with different beam steering angles are displayed in Figs. 23 and 24. Fig.23 displays the channel magnitude for different sized phased arrays with a beam steering resolution of 5° .

As CGP setup is considered, the main lobe of the Rx is always directed at Tx and DTs. As a result, higher channel magnitude values are recorded for the DL and joint DTs. The channel magnitude of the DI scattering components exhibits symmetric behavior around the crossover point. The channel magnitude increases until the crossover point as d_{bi} is decreasing. After the crossover point, the channel magnitude decreases until the end of the simulation due to an increase in the d_{bi} .

The channel magnitude of the 16x1 phased array is much higher than the 8x1 phased array, which is higher than the 4x1 phased array. The channel magnitude of the DI scattering components also exhibits a similar pattern. An interesting difference observed in the channel magnitude of the DL is that, when the angle between the vehicles approaches 90° (i.e., for the middle time of the simulation), the descent suffered by the 16x1 phased array setup is greater than rest of the setups. This is due to the narrower beams of this array and its higher gain within the scanning region (up to 60°). Moreover, the 16x1 setup results in slightly more fluctuations than 8x1 and 4x1 setups. This stems from the fact that 16x1 setup results in better spatial resolution (i.e., narrower beams) due to the larger number of AEs.

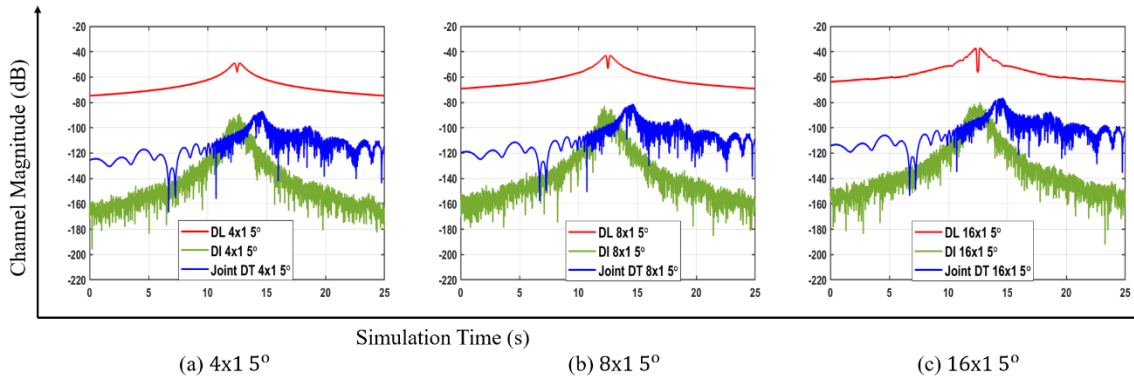


Figure 23. Phased arrays: Channel magnitude of DL, joint DTs, and DI scatterers

Similarly, the channel magnitudes of the different phased array setups with a beam resolution of 10° are shown in Fig.24. The DL is the strongest component, followed by joint DTs and DI scattering components in all setups. The 16x1 phased array setup outperforms the other setups in terms of channel magnitude. It results in higher channel magnitude. Again, the descent in the DL channel magnitude in the crossover interval is greater in the 16x1 setup compared to 8x1 and 4x1 setups. The DI scattering components show symmetric behavior around the crossover point. The channel magnitude of DI scattering component is also higher as higher gain values are obtained for 16x1 setup.

The channel magnitude pattern remains the same in 5° and 10° beam resolution setups. In all these setups, the DL is always the highest component. The joint DTs channel magnitude is always higher than the DI scattering component, except during the interval $11.5s \leq t_{sim} \leq 13.5s$. During this interval, DI scattering component is higher as the d_{bi} of some DI scatterers is lower than DTs, leading to higher channel magnitude values. The phased arrays with 10° beam resolution yield channel magnitudes overall lower than the 5° beam resolution setups. The 5° beam resolution setup considers a denser beam scanning grid, which, for the combining of all beams that we do, results in a flatter gain curve of the evaluated combined pattern, especially along the scanning region of $\pm 60^\circ$, which explains why the overall channel magnitude of the 5° resolution cases is flatter, i.e. has less ripples and fades than in the 10° cases.

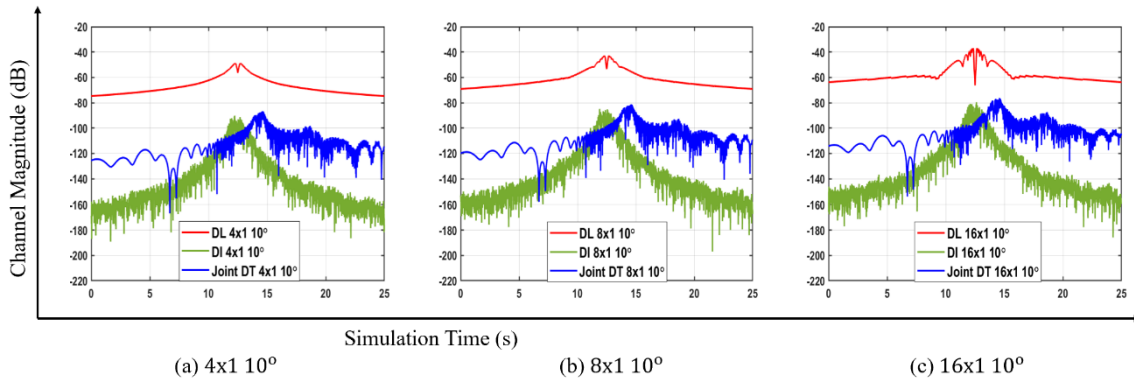


Figure 24. Phased arrays: Channel magnitude of DL, joint DTs, and DI scatterers

5.6.2 Overall Channel Magnitude

The overall channel magnitudes of different phased arrays with 5° and 10° beam steering resolution setups are shown in Fig.25. It is evident that the 16x1 setup results in better channel magnitude performance compared to 8x1 and 4x1 setups. For 5° and 10° beam steering resolution, the 16x1 setup achieves a channel magnitude that is 6dB and 12dB greater than those of the 8x1 and 4x1 setups, respectively. Similarly, 8x1 setup achieves a channel magnitude that is 6dB greater than that of 4x1 setup as shown in Fig.25.

As stated earlier, the phased array setups with 10° beam steering resolution result in relatively lower channel magnitude compared to the setup with 5° beam steering resolution. Furthermore, setups with a 10° beam steering resolution exhibit greater fluctuations in overall channel magnitude compared to those with a 5° beam steering resolution.

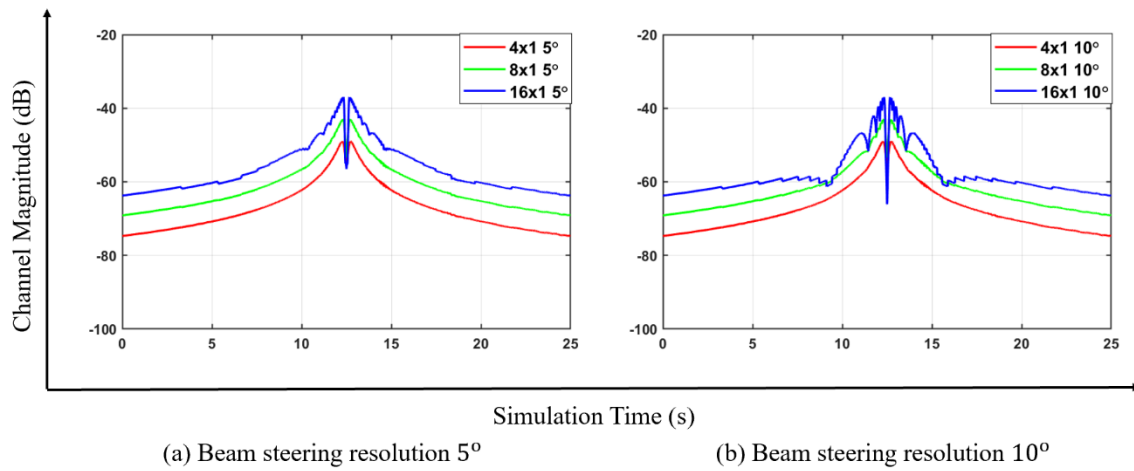


Figure 25. Phased arrays: Overall channel magnitude

5.6.3 Target Detection

The analysis of the DR for the various configurations of phased arrays reveals consistent performance across different setups, with minor differences driven by the array size and beam steering resolution. Increasing the array size from 4x1 to 16x1 shows a slight improvement in the average DR, with the 16x1 configuration achieving the highest average DR (79.17%) with a 10° beam steering resolution. However, the incremental gains between configurations such as 8x1 and 16x1 are marginal, indicating diminishing returns in detection performance with increasing array size.

Beam steering resolution also plays a significant role in target detection performance. Configurations with a 10° resolution consistently outperform those with a 5° resolution. This improvement is particularly evident in the 16x1 setup, where the wider beam steering resolution enhances coverage and leads to higher detection rates for specific targets. It ensures better detection of targets like PC2, which achieves the highest detection rate (83.64%) in the 16x1 10° configuration.

Target-specific trends highlight variations in detection performance. PC2 consistently achieves high detection rates across all setups, ranging from 82.76% to 83.64%, reflecting robust detection capabilities for this target type. In contrast, the Van demonstrates more variation, with detection rates ranging from 71.04% to 72.4%, suggesting it is more challenging to detect. This trend emphasizes the need for configuration optimization to warrant reliable detection across different target types.

The 16x1 array with a 10° beam steering resolution appears as the optimal configuration, offering the best trade-off between target detection capability and system design. It provides higher detection rates for challenging targets like the Van while maintaining robust detection performance across all targets. The results emphasize the importance of balancing array size and beamwidth to achieve consistent and reliable detection rates.

Table 6. DT detection rate for different phased arrays

Detection Rate (DR)	Bus	PC1	Van	PC2	Average DR
4x1 5°	74.4	86.6	71.8	83	78.95
4x1 10°	74.32	86.52	71.2	82.76	78.7
8x1 5°	74.04	86.4	71.04	83.08	78.64
8x1 10°	74.04	86.12	71.48	83.12	78.69
16x1 5°	73.96	85.84	72.08	82.84	78.68
16x1 10°	73.92	86.72	72.4	83.64	79.17

The snapshots indicate a similar phenomenon, reinforcing the trends observed in the detection rate analysis. These snapshots provide a visual confirmation of how the configurations influence the system's ability to detect and distinguish targets effectively. The target detection snapshots of different phased arrays with 5° and 10° beam steering resolution at $t_{sim} = 11.46s$ is given in Fig.26. At 11.46s, the vehicles have not crossed the Rx yet, indicated by the positive relative velocity value. As CGP setup is considered, the main lobe of the Rx is always directed at the Tx and DTs.

Figs. 26(a) and 26(d) show the target detection snapshot of a 4x1 phased array setup. The DL and all the DTs can be readily identified and distinguished from the clutter. The power levels in both the setups (5° and 10°) are almost identical. Similarly, the target detection snapshot of an 8x1 phased array setup is displayed in Figs. 26(b) and 26(e). The DL and DTs can be detected throughout most parts of the simulation. All the targets can be easily distinguished from the clutter. The power level of the 8x1 setup with 5° beam steering resolution is higher compared to the 10° setup. This power level difference can be observed in the DL from Tx. Figs. 26(c) and 26(f) shows the target detection snapshot of a 16x1 phased array setup. In the given setup, all targets of interest can be successfully identified and distinguished from the clutter. In terms of power levels, the 5° beam steering resolution setup results in higher power compared to the 10° beam steering resolution setup. This variation in power levels is much more significant compared to the 8x1 setup. The power level difference is recorded for the DL and all the DTs in the scenario. A few high-power DI scatterers can also be observed, indicating that higher power levels are also recorded for DI scatterers in the 5° beam steering resolution setup.

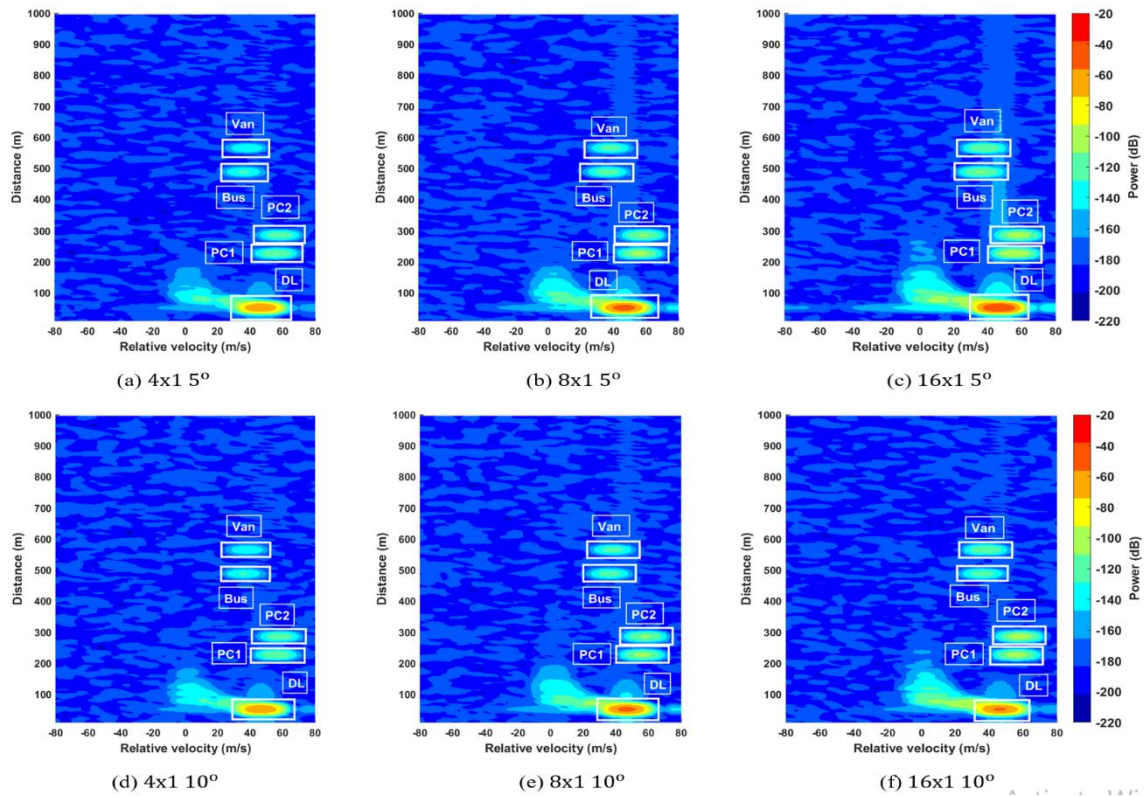


Figure 26. Phased arrays: Target detection snapshot at 11.46s

In a similar way, the target detection snapshots at $t_{sim}= 13.56s$ is shown in Fig.27. At 13.56s, the Rx and Tx crossed each other, indicated by the change from positive to negative relative velocity value of the DL. On the other hand, the DTs have not yet crossed the Rx. There is no change in the relative value of velocity.

The target detection snapshot of 4x1 phased array setup at $t_{sim}= 13.56s$ is given in Figs. 27(a) and 27(d). The power levels of the DL and DTs are sufficient for their successful identification and detection. The DL is the strongest component indicated by the higher power level in the snapshots. The power levels of PC1 and PC2 are higher than Bus and Van because of the lower d_{bi} . The power levels of the DL and DTs in 5° and 10° setups are almost identical. However, the power level of DI scatterers is higher in 5° setup as the snapshot shows more high-power DI scatterers. Similarly, the target detection snapshots of 8x1 phased array are given in Figs. 27(b) and 27(e). The targets of interest can be readily identified in these snapshots. The power levels of the DL and DTs are sufficient for their successful detection. They can be easily distinguished from the clutter. The power level of DL and DTs is higher in 5° setup compared to the 10° setup. It can be clearly seen that DL and DTs benefit from the narrower scanning angle of the 5° setup, which provides equal or higher gain in all directions and better focus on the signal path. Figs. 27(c) and 27(f) show the target detection snapshots of the 16x1 setup. The main lobe of the Rx is always directed at the Tx and DTs, leading to higher power levels for them. The DL and DTs can be successfully identified and distinguished from the clutter in the environment. The power levels recorded in the 5° setup are higher than the 10° setup. The power level difference is significantly higher than the other setups. This indicates the high directional gain with the narrower beamwidth. Thus, a 5° beam steering resolution setup results in higher power levels and better target detection accuracy compared to a 10° beam steering resolution setup.

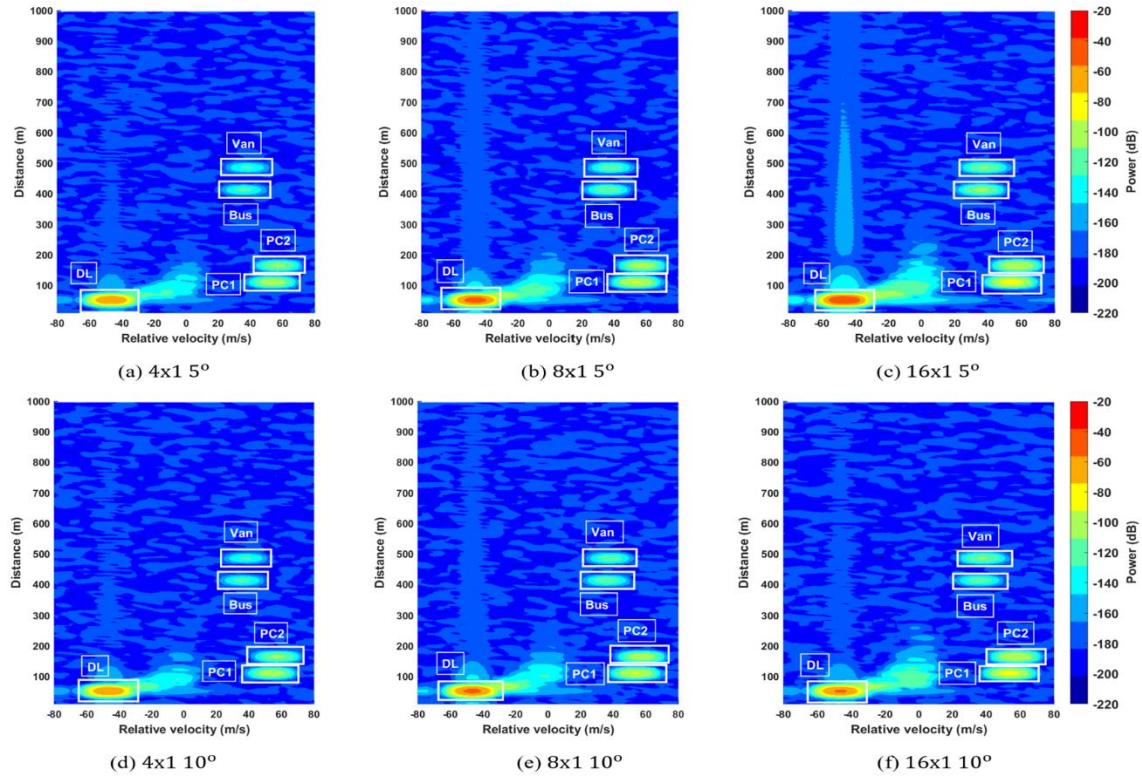


Figure 27. Phased arrays: Target detection snapshot at 13.56s

5.6.4 Statistical Characteristics of Different Phased Arrays

The statistical characteristics of different phased arrays are given in Table 7. It provides a comparison of the channel magnitude values of DL, DTs, and DI scattering components for the considered phased arrays. Moreover, the coefficient of variation value provides insights into the variation of the channel magnitudes with respect to their means.

The 16x1 phased array achieves the highest channel magnitude of the DL when compared to the 8x1 and 4x1 phased arrays. Specifically, it exhibits a difference of 5.27dB and 4.15dB relative to the 8x1 phased array for the 5° and 10° setups, respectively. For the joint DTs, the 16x1 configuration provides a gain of 5.18dB and 4.61dB for the 5° and 10° setups, respectively. Regarding the DI scattering components, the 16x1 phased array demonstrates a gain of 5.16dB and 4.68dB for the 5° and 10° setups, respectively.

The disparity in channel magnitude values becomes even more pronounced when the 16x1 phased array is compared to the 4x1 phased array, highlighting the superior performance of the larger array configuration. In the case of DL, 16x1 setup yields a gain of 10.86dB and 9.47dB for the 5° and 10° setups, respectively. Similarly, a difference of 10.74dB and 10.1dB is recorded in the joint DTs channel magnitude values for the 5° and 10° setups, respectively. For DI scattering components, the 16x1 phased array demonstrates a gain of 10.51dB and 10.3dB for the 5° and 10° setups, respectively.

Similarly, the 8x1 phased array outperforms the 4x1 phased array in terms of channel magnitude. For the DL, the 8x1 setup achieves gains of 5.59dB and 5.32dB for the 5° and 10° setups, respectively. In the case of joint DTs, the recorded differences are 5.56dB and 5.4dB for the 5° and 10° setups, respectively. For DI scattering components, the 8x1 phased array provides gains of 5.35dB and 5.61dB for the 5° and 10° setups, respectively.

The analysis highlights that larger phased arrays (16x1 and 8x1) consistently outperform smaller ones (8x1 and 4x1) in terms of channel magnitude across all setups and components (DL, joint DTs, and DI scatterers). The 16x1 phased array delivers the highest gains, demonstrating a significant advantage, while the 8x1 phased array also provides notable improvements over the 4x1 setup. In fact, we observe diminishing returns, since going from 4 AEs to 8 AEs provides larger increases in channel magnitudes of DL, DTs and DI scatterers than going from 8 AEs to 16 AEs. On the other hand, smaller beam steering resolutions (5°) yield slightly higher gains compared to 10° setups for 4 and 8 AEs, while they provide a more noticeable increase for the case with 16 AEs. The differences in terms of coefficient of variation are smaller than the ones observed among the horn antenna, patch antenna, and not very relevant, except for the 16 AEs case, where the beam steering resolution has impact on the coefficient of variation, particularly for the DL. This is due to the more irregular pattern within the $\pm 60^\circ$ scanning region of the 10° resolution pattern.

On the other hand, it is worth noting that, unlike when going from the phased array AE to the patch antenna, and then to the horn antenna, here we have a lower increase in the magnitude of the DTs than the increase in magnitude of the DI scatterers when we increase the number of AEs. This means that our clutter level is relatively larger than our DTs level, which could lead to DTs masking. However, it is still larger enough to not pose a problem in terms of target detection in the considered scenario. This is shown in the average target DR, which implies that it is generally possible to detect the targets throughout the simulated scenario. Regarding this FoM, we observe an extremely similar performance among all the considered arrays and beam steering resolutions, for all targets. The reason behind this is that the increase in “useful” signal (IDL-DTs) when resorting to more AEs comes with an equivalent increase in “interference” (IDL-DI) because the higher gain of the arrays with more AEs affects both components roughly the same. On another note, the lower beam steering angular resolution arrays with 8 and 16 AEs yield slightly better target DR. The reason for this could be illustrated by looking at the 16x1 array radiation pattern from Fig. 10. There, we can see that the 10° beam steering angular resolution array has quite lower gain values towards the 90° of azimuth (side of the Rx vehicle). This angular area is not so interesting to cover (i.e. to have higher gain), at least in terms of results averaged throughout the simulation, because it will increase the reception of energy coming from the DI scatterers, located at the sides of the Rx vehicle), while the increase in energy coming from the backscattering of the DTs will not be that much (again, if we average over all the simulation time) because the time in which the DTs will be in those angles (around 90°) is much shorter than the time they will be in angles closer to 0° and 180°.

Finally, if we compare the phased array results to those of the other considered antennas, we have that the horn antenna provides solid performance, since it is roughly the same in terms of DL and DTs magnitudes as the 16x1 array with 10° beam steering resolution, but it has a much lower magnitude of DI scatterers, which is positive for sensing the DTs. In addition, it has a much lower coefficient of variation in the DL, which is positive. It is also much lower for the DI scatterers, being this alone not positive, but, since we have 10 dB less on average, it is not worse overall. Therefore, only the 16x1 array with 5° beam steering resolution comes on top in terms of DL and DTs magnitudes, applying the same points as the ones from the comparison of the horn antenna against the 16x1 array with 10° beam steering resolution. This good performance of the horn antenna can partially be uplifted by the fact that ideal materials and no mismatch losses have been considered. However, it is also due to horn antennas producing a radiation pattern which is much more concentrated in the azimuthal plane than that of patch antennas.

Therefore, depending on how relevant we consider the radiation outside the azimuthal plane, it could be a good option to use a horn antenna as the AE for creating an array and investigating its performance, or consider 2D arrays which are also selective in elevation, thus concentrating more energy in the azimuthal plane (or where required, steering the beam also in elevation).

In terms of DR, if we compare Table 5 and Table 7, we can see that the phased arrays do not perform better than any other of the considered antennas in the CGP setup. This is, as explained in the paragraph prior to the above, a consequence of the fact that the increase in “useful” signal (IDL-DTs) that we can achieve with (some) phased array configurations comes with an equivalent increase in “interference” (IDL-DI) because the higher gain of the arrays affects both components roughly the same. This is also because of how we have defined the radiation pattern of the arrays, in which we have combined all beam patterns, making the combined pattern no longer very spatially selective. In fact, the scanning angles considered ($\pm 60^\circ$ in this case) can also have an impact on these results with how we have composed the combined radiation pattern. This highlights the need for future work in which the performance gains of the phased arrays can be characterized more accurately.

Table 7. Statistical properties of different phased arrays

Type	Mean (dB)			Coefficient of Variation			Average DR
	DL	IDL-DTs	IDL-DI	DL	IDL-DTs	IDL-DI	
4x1 5°	-64.31	-108.63	-120.23	1.09	1.65	3.17	78.95
4x1 10°	-64.39	-108.69	-120.49	1.1	1.65	3.16	78.7
8x1 5°	-58.72	-103.07	-114.88	1.11	1.64	3.17	78.64
8x1 10°	-59.07	-103.29	-114.87	1.12	1.66	3.14	78.69
16x1 5°	-53.45	-97.89	-109.72	1.14	1.61	3.04	78.68
16x1 10°	-54.92	-98.68	-110.19	1.23	1.66	3.27	79.17

6 Conclusion

This deliverable evaluates antenna placement schemes, radiation patterns, and phased array configurations to optimize the performance of ISAC-enabled V2V systems. A novel propagation model was developed and tested in a highway scenario, using channel magnitude and target detection accuracy as key performance metrics. Recognizing the critical role of diffuse scatterers, they were integrated into modeling to reflect real-world conditions, where their high-power clutter poses challenges for precise target detection.

Simulations demonstrated that Combined Gain Pattern (CGP) configurations consistently outperform single front or rear bumper setups, achieving higher channel magnitudes and superior target detection. Among single antennas, horn antennas delivered the best results.

Phased arrays further enhanced system performance in terms of channel magnitudes, but not in terms of average DR. Configurations with larger arrays (e.g., 16x1) and finer beam steering resolutions (5°) provided significant improvements in channel magnitude and detection accuracy, thanks to their superior directional gain and reduced signal fluctuations. Smaller arrays and coarser beam resolutions, while effective, were comparatively limited in performance.

The findings highlight phased arrays as a pivotal technology for future ISAC-enabled V2V systems, addressing the stringent demands of 5G and beyond. By improving traffic safety, reducing congestion, and enabling intelligent transportation systems, this research underscores the transformative potential of phased arrays in advancing vehicular communication and sensing technologies.

However, only one of all the considered arrays (16x1 with 5° beam steering resolution) was able to outperform the horn antenna in terms of channel magnitudes. While some simulation differences should be addressed, it highlights the relevance of choosing the right antenna design for the right application, since the good performance of the horn antenna is explained by its selectivity in the elevation plane. It is left for future work to investigate how relevant radiation coming or being transmitted outside the azimuthal plane is, and adapt the antenna design accordingly, either using horn antennas as AEs for a linear array, or keeping the easier to integrate patches, but resort to 2D arrays which are also selective in elevation.

It is also left for future work the development of a more refined simulation framework that can properly capture aspects such as the array switching times, the scheduling of an ISAC system, including practical aspects, such as how often it is needed to detect a target, as well as the evaluation and comparison of analog, hybrid, and digital beamforming for ISAC systems. All this would be able to obtain a performance estimation closer to reality, especially regarding the target DR, without needing to resort to some of the assumptions present in this deliverable, particularly regarding the CGP and the phased array combined patterns.

The final point of future research is the consideration of several aspects regarding target detection, such as noise or receiver sensitivity. On the other hand, the target DR FoM could be improved by developing a weighting scheme for the different targets, accounting for several variables such as the distance to the targets, and their relative speed and direction.

References

- [1] F. Liu *et al.*, “Integrated Sensing and Communications: Toward Dual-Functional Wireless Networks for 6G and Beyond,” *IEEE Journal on Selected Areas in Communications*, vol. 40, no. 6, pp. 1728–1767, Jun. 2022, doi: 10.1109/JSAC.2022.3156632.
- [2] Z. Wei *et al.*, “Integrated Sensing and Communication Signals Toward 5G-A and 6G: A Survey,” *IEEE Internet Things J*, vol. 10, no. 13, pp. 11068–11092, Jul. 2023, doi: 10.1109/JIOT.2023.3235618.
- [3] A. Liu *et al.*, “A Survey on Fundamental Limits of Integrated Sensing and Communication,” *IEEE Communications Surveys and Tutorials*, vol. 24, no. 2, pp. 994–1034, 2022, doi: 10.1109/COMST.2022.3149272.
- [4] R. S. Thomä *et al.*, “Cooperative Passive Coherent Location: A Promising 5G Service to Support Road Safety,” *IEEE Communications Magazine*, vol. 57, no. 9, pp. 86–92, Sep. 2019, doi: 10.1109/MCOM.001.1800242.
- [5] J. Mu, Y. Gong, F. Zhang, Y. Cui, F. Zheng, and X. Jing, “Integrated Sensing and Communication-Enabled Predictive Beamforming With Deep Learning in Vehicular Networks,” *IEEE Communications Letters*, vol. 25, no. 10, pp. 3301–3304, Oct. 2021, doi: 10.1109/LCOMM.2021.3098748.
- [6] D. Cong, S. Guo, S. Dang, and H. Zhang, “Vehicular Behavior-Aware Beamforming Design for Integrated Sensing and Communication Systems,” *IEEE Transactions on Intelligent Transportation Systems*, vol. 24, no. 6, pp. 5923–5935, Jun. 2023, doi: 10.1109/TITS.2023.3251303.
- [7] R. He *et al.*, “Propagation Channels of 5G Millimeter-Wave Vehicle-to-Vehicle Communications: Recent Advances and Future Challenges,” *IEEE Vehicular Technology Magazine*, vol. 15, no. 1, pp. 16–26, Mar. 2020, doi: 10.1109/MVT.2019.2928898.
- [8] D. S. Baum, J. Hansen, G. d. Galdo, M. Milojevic, J. Salo, and P. Kyosti, “An Interim Channel Model for Beyond-3G Systems Extending the 3GPP Spatial Channel Model (SCM),” in *2005 IEEE 61st Vehicular Technology Conference*, IEEE, pp. 3132–3136. doi: 10.1109/VETECS.2005.1543924.
- [9] J. Meinilä, P. Kyösti, T. Jämsä, and L. Hentilä, “WINNER II Channel Models,” in *Radio Technologies and Concepts for IMT-Advanced*, Wiley, 2009, pp. 39–92. doi: 10.1002/9780470748077.ch3.
- [10] W. Anwar, N. Franchi, and G. Fettweis, “Physical Layer Evaluation of V2X Communications Technologies: 5G NR-V2X, LTE-V2X, IEEE 802.11bd, and IEEE 802.11p,” in *2019 IEEE 90th Vehicular Technology Conference (VTC2019-Fall)*, IEEE, Sep. 2019, pp. 1–7. doi: 10.1109/VTCFall.2019.8891313.
- [11] T. Abbas, J. Karedal, and F. Tufvesson, “Measurement-Based Analysis: The Effect of Complementary Antennas and Diversity on Vehicle-to-Vehicle Communication,” *IEEE Antennas Wirel Propag Lett*, vol. 12, pp. 309–312, 2013, doi: 10.1109/LAWP.2013.2250243.
- [12] J. Karedal *et al.*, “A geometry-based stochastic MIMO model for vehicle-to-vehicle communications,” *IEEE Trans Wirel Commun*, vol. 8, no. 7, pp. 3646–3657, Jul. 2009, doi: 10.1109/TWC.2009.080753.

- [13] J. Zhang *et al.*, "Integrated Sensing and Communication Channel: Measurements, Characteristics, and Modeling," *IEEE Communications Magazine*, vol. 62, no. 6, pp. 98–104, Jun. 2024, doi: 10.1109/MCOM.020.2300165.
- [14] Z. Zhang *et al.*, "A General Channel Model for Integrated Sensing and Communication Scenarios," *IEEE Communications Magazine*, vol. 61, no. 5, pp. 68–74, May 2023, doi: 10.1109/MCOM.001.2200420.
- [15] A. U. Khan, S. N. Haider Shah, C. Schneider, and J. Robert, "Target Detection in a Highway Scenario with Extended V2V Channel Model," in *2024 IEEE Wireless Communications and Networking Conference (WCNC)*, IEEE, Apr. 2024, pp. 1–6. doi: 10.1109/WCNC57260.2024.10571136.
- [16] A. U. Khan, N. D. Chaudhury, S. N. H. Shah, C. Schneider, and J. Robert, "Impact of Antenna Position and Radiation Patterns on Target Detection in a Highway Environment Utilizing ICAS Extended Model," in *2024 IEEE Vehicular Networking Conference (VNC)*, IEEE, May 2024, pp. 140–147. doi: 10.1109/VNC61989.2024.10576005.
- [17] D. Quack, M. Meuleners, S. Hommen, and C. Degen, "Simulation-based evaluation of MIMO antenna systems in car-to-car communication," in *The 8th European Conference on Antennas and Propagation (EuCAP 2014)*, IEEE, Apr. 2014, pp. 3049–3052. doi: 10.1109/EuCAP.2014.6902470.
- [18] N. D. Chaudhury, L. Berkelmann, B. Janssen, and J. Robert, "Weighted Partial Radiation Efficiency and Effective Coverage as Key Performance Indicators for the Analysis of Automotive Antennas," in *2023 IEEE Conference on Antenna Measurements and Applications (CAMA)*, IEEE, Nov. 2023, pp. 677–680. doi: 10.1109/CAMA57522.2023.10352819.
- [19] N. D. Chaudhury, L. Berkelmann, B. Janssen and J. Robert, "On Vehicular Model Reduction for Antenna Simulation Using Spherical Wave Expansion," *2023 IEEE International Symposium on Antennas and Propagation and USNC-URSI Radio Science Meeting (USNC-URSI)*, Portland, OR, USA, 2023, pp. 935-936, doi: 10.1109/USNC-URSI52151.2023.10238108.
- [20] Y. Wang, X. Wang and F. Yuan, "Design and Implementation of 24GHz Series Fed Microstrip Antenna Array for Automotive Radar," *2022 14th International Conference on Measuring Technology and Mechatronics Automation (ICMTMA)*, Changsha, China, 2022, pp. 887-890, doi: 10.1109/ICMTMA54903.2022.00181.
- [21] Q. Tan, K. Chen, K. Fan and G. Luo, "A Low-sidelobe Series-fed Microstrip Patch Antenna Array for 77 GHz Automotive Radar Applications," *2020 Cross Strait Radio Science & Wireless Technology Conference (CSRSWTC)*, Fuzhou, China, 2020, pp. 1-3, doi: 10.1109/CSRSWTC50769.2020.9372542.
- [22] R. G. Zarnagh and A. Alayón Glazunov, "Correlation and Non-Orthogonality Figures of Merit of Beamforming Fields," *2023 17th European Conference on Antennas and Propagation (EuCAP)*, Florence, Italy, 2023, pp. 1-5, doi: 10.23919/EuCAP57121.2023.10133475.